공학박사 학위논문

Mechanical stress engineering for the shape design of DNA origami structures

DNA 오리가미 구조체의 형상 설계를 위한 기계적 응력 조절 기술

2020년 2월

서울대학교 대학원

기계항공공학부 기계공학전공

김 영 주

Abstract

In this thesis, we describe two design strategies that engineer mechanical stress to program static or dynamic conformations of the DNA origami structure. DNA origami nanotechnology facilitated the self-assembly of DNA strands into any conceivable shape encoded by their rationally designed sequences. Mechanics-based design approaches have played an important role in improving the structural diversity of the DNA origami structures. Due to low twist controllability and limited reconfiguration mode, however, they have still limitations in achievable diversity or complexity in structural shapes and their reconfigurations and their applications. To this end, first, we developed a design strategy for fine control of twisted DNA origami structures by considering not only amount of geometrical perturbations but also their arrangements within the structures. With the configurational design of geometrical perturbations, we can program various distributions of the mechanical stress enabling a fine control over twist rate of DNA origami structures. Second, we developed a design strategy that transforms a two-dimensional structure into three-dimensional supercoiled one on demand. We employed the topological invariant property to convert a simple twist deformation into complex bending one leading to supercoiling of the DNA origami structure. We expect that our mechanical stress programming strategies can be utilized to design DNA origami structures with desired shapes or reconfiguration motions and enhance the performance of functional structures.

Keywords: DNA origami, DNA nanostructure, Mechanical stress engineering, Twist control, Reconfigurable nanostructure, Mechanical instability

Student Number: 2013-20654

Table of contents

List of tables

List of figures

Chapter 1. Introduction

1.1. Research background

1.1.1. DNA origami nanotechnology

Well known as a carrier of genetic information, Deoxyribonucleic acid (DNA) is a biological macromolecule ubiquitous in all living organisms. One of the most prominent features of DNA is the Watson-Crick base-paring interaction between two complementary bases (A with T and C with G) leading to formation of double helices[1]. It makes it possible for various interactions with high specificity to be designed with only permutation of nucleobase sequences of DNA strands. The programmability and the specificity of the interactions make DNA a powerful engineering material laying the foundation of DNA nanotechnology.

In 1982, the potential of DNA as the engineering nanomaterial was demonstrated by the Seeman's seminal work. He showed that a rationally designed sequences of DNA strands can program shape and interactions of a nanoscale building block producing the 3D DNA crystal[2]. Inspired by his pioneering work, a number of researchers have developed various strategies for designing DNA nanostructures with designed shapes.

The most successful approach is the DNA origami method suggested by Rothemund in 2006[3]. The DNA origami folds a long, circular single-stranded DNA (ssDNA), called scaffold strand, into arbitrary custom two-dimensional geometries with hundreds of short ssDNA, called staple strand, through the self-assembly of

strands (Fig. 1-1). To hold the scaffold strand in place along the target shape, staple strands bind to the pre-defined positions directed by their sequences forming double helices. The adjacent, parallel helices were periodically connected by an inter-helix junction, called crossover. Its position was carefully determined by considering the helicity (10.5 base-pair per turn) of a canonical B-DNA to avoid unwanted shape distortions. In addition to the high shape programmability, the DNA origami provides high folding yield since a long scaffold strand was employed to organize multiple staple strands without the problem of stoichiometry of staple strands[4]. Later, this methods was extended to custom three-dimensional geometries by approximating them as parallel and straight double helices constrained on a honeycomb[5] or a square lattice[6], the lattice-based DNA origami, significantly improving its design capability.

Coupled with the ability to attach other functional components including proteins, nanoparticles, fluorophores, carbon nanotubes (CNTs) and etc., the static DNA origami structure can serve as nanoscale templates to organize them with high spatial addressability. It has been widely utilized for developing biophysical experiment tools with high controllability[7-8], and electronic[9-10] or nanophotonic DNA devices[11-12] with programmable properties. With integration of stimuli-responsive elements, furthermore, DNA origami structures can be utilized as a dynamic system that can reconfigure its conformational shape enabling development of biological sensors or functional nanorobots. For example, a smart drug delivery system showed its great promise[13]. Recognizing target molecules on the cell membrane, it changes its structure to release payload.

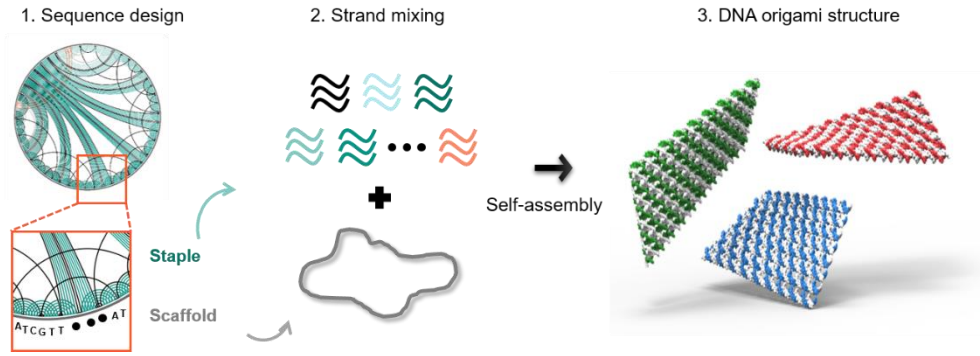

Figure 1-1. A schematic illustration of design process of DNA origami nanostructures.

1.1.2. Self-assembly of DNA origami structure

Synthesis of DNA origami structures is achieved through self-assembly of a scaffold strand and up to 200 staple strands whose length ranges from 20 to 50 nucleotides (NTs). Size of DNA origami structures depends on length of the scaffold strand used. Typically, the ssDNA with length of 7249 NTs, M13mp18, derived from *E. coli*, is most widely used[3]. To make larger structures, variants of M13mp18 with length of up to 8634 are used[5]. Also, the limit of size can be overcome via hierarchical assembly of DNA origami monomers using sticky ends[14], blunt ends[15], and shape complementarity[16-17]. Sequence of staple strands is determined to have complementary one at their binding position.

To ensure the self-assembly of strands occur, generally, excessive amount of staple strands is mixed with the scaffold strand (e.g., 5 to 10 times higher concentration than that of the scaffold strand). Also, the solution for self-assembly includes the pH buffer like Tris-Acetate-EDTA (TAE) or Tris-Borate-EDTA (TBE) and salt such as sodium or magnesium to mitigate electrostatic repulsion between DNA helices whose phosphate backbone atoms have negative charges. For successful folding, salt concentration should be carefully selected. If salt concentration is low, structures would not be successfully folded since large repulsion forces hamper closed packing of negatively charged helices. If salt concentration is large, otherwise, then structure would be aggregated. Therefore, determination of optimal salt concentration, which is also structure-dependent, is necessarily required for self-assembly with high yield.

Self-assembly for DNA origami structures is conducted through the thermal annealing process. First, the temperature of the reaction solution is increased up to

85 to 90 ºC in order to break undesired hybridization between strands. Then, the solution slowly cools down to 25 ºC for a long time, up to a few days. However, researchers found that folding of DNA strands can be achieved at isothermal condition even within an hour[18], enabling rapid synthesis of DNA origamis structures.

Folding quality of folded structure need to be checked via agarose gel electrophoresis. If successful, a distinct monomer band should be observed. Varying salt condition and annealing process, optimal conditions for those should be determined to ensure well-formed structures with high yield. Detailed protocols for initial folding screen are provided in the literature[19]. Then, structural shape can be characterized using atomic force microscope (AFM), transmission electron microscope (TEM) or cryo-TEM.

1.1.3. Structural motifs

Structural shape and mechanical properties of the DNA origami structure depend on those of their constituents, including dsDNA, crossover, nick, gap, and ssDNA entropic spring. Therefore, it is important to understand their structural and mechanical properties for achieving DNA origami structures with desired properties.

Most of the structure consists of dsDNA. It has a form of double helix with axial rise of 0.34 nm and helicity of 10.5 BP/turn. Therefore, both length and twist angle along the helical axis are changes when the number of BP is changed. Also, its mechanical properties including stretch, bending, twist and coupling between them were well characterized by various single molecule experiments[20-22].

Adjacent dsDNAs are connected by an inter-helix junction, called crossover. To avoid unwanted deformation of DNA origami structures, the position of crossovers should be carefully determined by minimizing geometrical mismatches for both stretch and twist between adjacent helices since dsDNA is a helical structure. Double crossover exists in the form of the Holliday junction (HJ) in the DNA origami structure. When only the HJ exists in solution without constraints, it is known to form a stacked right-handed conformation with a ~60º inter-helical angle due to electrostatic repulsion between dsDNAs[23-25]. According to results from molecular dynamics simulation for DNA origami structures[26-27], however, it showed parallel or even slightly left-handed twisted conformations implying that structural deformation of HJs might occur due to its high flexibility[28-30].

Since multiple staples strands are used, there are breaks in phosphate backbone where the 5’ end and the 3’ end of different staple strands meet, called nicks. The nick is known to reduce torsional rigidity through the relaxation of

backbone[31]. Since effect of the nick is sequence-dependent, rational design of location of nicks can be utilized to finely control twisted shape of DNA origami structures[31].

By replacing staple strands at nicks with shorter staple strands, short (3 to 5 NTs) unpaired ssDNA, called gap, can be obtained. Since ssDNA is much flexible compared to dsDNA, it can be used to reduce stiffness of DNA origami structures without change in structural shape by rationally designing its distributioin[32]. When the length of ssDNA is long, on the other hand, it can act as an entropic spring that generates forces to deform DNA origami structures by tension[33-35].

Depending on how these structures motifs are arranged, various structural shapes and mechanical properties can be designed, which can be achieved by simply designing sequences of staple strands.

1.1.4. Computational design and analysis tools

To aid in the design process of the DNA origami structure, several computational tools were developed. They significantly lowered an entry barrier to the DNA origami nanotechnology making it the most widely used approach in the fabrication of DNA nanostructures.

In sequence design of the lattice-based DNA origami structures, for example, a CAD software specialized for DNA origami structure, caDNAno, aided in the design of sequences and shapes by providing an interactive interface for design. Since it assumes that all helices are parallel existing on the honeycomb or the square lattice, however, it was difficult to design structures like wireframe shapes. Recently, this problem was recently resolved by advanced computational algorithms[36-39]. For example, the DEADALUS (DNA origami Sequence Design Algorithm for User-defined Structures) can determine automatically a routing of the scaffold strand and provide corresponding sequences of staple strands[37] when a target wireframe structure is given as the CAD file like PLY (Polygon File Format).

In addition to experimental characterization such AFM, TEM and cryo-EM, the designed structures can be characterized through computational methods. There were many attempts to accurately predict shape of the designed structures using coarse-grained model[40] or MD simulation[26]. Since size of structures is too large to be analyzed using them, however, a more efficient analysis tool was required to provide feedback to design. Therefore, the computational framework (CanDo) was developed to rapidly predict the three-dimensional shape and flexibility of the designed DNA origami structures[41-43] using the finite element analysis (FEA). It is a continuum model at base-pair level abstracting dsDNA into a structural beam with

the structural and mechanical properties of dsDNA and considering inter-connections between adjacent helices as structural constraints[41-42]. Since structural and mechanical information is compressed at base-pair level, however, more detailed dynamic properties and atomic-level information should be obtained through oxDNA or MD simulation.

1.2. Design strategy for DNA Origami structure

1.2.1. Lattice-based design

When proposed by P. Rothemund in 2006[3], the DNA origami method determines location of crossovers assuming that helices exist in a plane. Due to the limited design rule for crossover, this method cannot be easily extended into three dimensional structures. In 2009, S. Douglas provided a straightforward design rule to construct three dimensional DNA origami structures[5] by constraining position of helices onto a honeycomb lattice. Considering the helicity of B-DNA (10.5BP per turn), crossovers exist every 7 BPs and their directions rotates 240 º every 7 BP along the axial axis, resulting in arrangement of helices on the honeycomb lattice. Therefore, a certain double helix can be connected to up to three adjacent double helices in parallel without geometrical mismatches. This design principle makes it easy to construct straight DNA bundles with various cross-sectional shapes. Later, structures were also designed on a square lattice or hybrid lattices by using finely controlled crossover spacing rules[6, 44]. Although crossovers are regularly arranged, crossover spacing rules for them, which are inconsistent with the helicity of B-DNA, make structural deformation. In case of the square-lattice, for example, crossovers exist every 8 BP and a certain helice can be connected up to 4 helices, and structures on the square lattice experience left-handed twist of the global structure.

1.2.2. Flexible hinge-assisted design

To achieve the static structure with desired shapes and the dynamic structure with coordinated motions for DNA origami structure, a variety of design strategies have been utilized. The typically employed method is using ssDNA. Through a utilization of ssDNA to form multiway junctions, more complex structural shapes like wireframe structures can be constructed by the DNA origami method[36-39, 45-46]. Due to the high flexibility of ssDNA, it can serve as multiway junctions connecting edges (single or multiple dsDNA) with the desired angle. Although the presence of multiple multiway junctions made it difficult to manually determine the scaffold routing, recently, the several algorithmic design approach resolved the problem[36-39, 46]. In addition to expanding structural diversity of the static DNA origami structure, ssDNA can also serve as a flexible hinge to be easily deformed in the dynamic DNA origami structure, enabling implement of reconfigurations with complex, coordinated motion[47-48]. Giving degree-of-freedoms for relative motions between different stiff dsDNA bodies, the ssDNA hinge also constrains trajectories of the dsDNA bodies. Combining multiple ssDNA hinges and appropriate triggers, therefore, various coordinated on/off switching motions of DNA origami structures were demonstrated[47-48].

Although the ssDNA provided high potentials in both the static and the dynamic DNA origami structures, however, the flexibility of ssDNA makes its utility limited. The structures with ssDNA multiway junctions or hinges are subject to large conformational fluctuations reducing the advantages as the structural templates to accurately control materials. Also, an intermediate conformation between the open and the close ones cannot be well controlled.

1.2.3. Mechanical stress-assisted design

Alternatively, mechanical stress as an active source to deform dsDNA bodies can be employed to achieve both the static shape with and the reconfiguration into the desired conformations without loss of structural stiffness.

Interestingly, ssDNA as an entropic spring was the first approach to generate mechanical force to apply tensional forces at predefined positions. Its use was demonstrated through construction of the DNA tensegrity[33] and the bent multi-helix bundles with the desired angle[34-35]. The entropic force of ssDNA is controlled by its number of the nucleotides and its end-to-end length. Since they are determined during the sequence design phase, however, it is difficult to apply it in reconfiguring structures.

Later, a concept of 'geometrical perturbation' was suggested to generate internal mechanical stress leading to conformational changes of the DNA origami structure. As well as in the sequence design process, this principle can be implemented even after self-assembly of strands enabling reconfiguration of the dynamic DNA origami structure. The geometrical perturbation occurs when the constraints rendered by crossover are not satisfied. To avoid unexpected shape distortions, in fact, the positions of the crossovers connecting the helices in the DNA origami structures should be carefully determined with consideration on the geometry of B-DNA (axial rise of 0.34 nm per base-pair, and helicity of 10.5 base-pair per turn) and relative positions between two adjacent helices. The position of the crossovers renders constraints on the distance and the twist angle along a certain helix between neighboring crossovers. If these constraints are not satisfied, deformation of helices would be required to form crossovers resulting in internal

mechanical stress within the structure.

Strategies to generate geometrical perturbations in the structure can be divided into two main categories. For the design of the static structure with the desired shape, first, the mechanical stress can be encoded in the sequence design phase that determines connectivity of staple strands and their sequences[27, 49-50]. During the sequence design, base-pair (BP) insertions or deletions can be introduced into the straight reference structure. Then, they cause geometrical perturbations making the straight structure bent and twisted to minimize the geometrical perturbations at crossover positions. The number of BP insertions and deletions can control amount of curvatures and twist rates of the DNA origami structure.

On the other hand, the mechanical stress for the reconfigurable structure can be encoded through additional reactions that change the geometry of B-DNA, leading to geometrical perturbations, after the self-assembly. For example, UV light can be used to reduce twist angle between two neighboring BPs due to photo-lesions[51]. However, this reaction makes irreversible structural deformation so that a reversible reconfiguration cannot be achieved. Alternatively, use of DNA binding molecules like Ethidium Bromide (EtBr) can be employed to generate geometrical perturbations on-demand after the self-assembly of strands. EtBr binding to DNA is known to reduce twist angles as well as increase distances between neighboring BPs[52] and its binding is reversible. Bound to DNA origami structures, EtBr would generate torsional stress within the structures since torsional degree-of-freedoms of each helix are constrained by crossover. This torsional stress would make structures twisted along their axial axis since EtBr would uniformly bind to them. By varying concentration of EtBr, therefore, reversible twist control of multi-helix bundles can

be achieved [53-54].

1.3. Research motivation

Although the mechanical stress encoding strategy has useful advantages, however, the conventional approaches for it have some limitations in their use.

In the design of the static structure, first, with only change of the number of BP insertions and deletions, it is difficult to achieve fine control over the twist rate. While the use of BP insertions or deletion is quite simple and effective in designing diverse structural shapes, it has an intrinsic limitation in that only natural numbers of BP insertion and deletion can be used resulting in discrete values of twist rate achievable, leading to low controllability over the twist rate. Contrast to curvature control[49], especially, a design method for precise twist control has rarely been found hampering a development of automatic shape design approach for achieving three dimensional curves with both target curvature and twist rate. The low controllability over the twist rate in DNA origami structures limited theirs use in various application. For example, Twisted ones have demonstrated their abilities to tune the release kinetics of intercalating drugs[55] and modulate the macroscopic structure and elastic properties of chiral colloidal liquid crystals[56]. In addition, twist control was found to be important in building a polymeric superstructure into a target shape[17, 49, 57]. Fine control over these structural features is, therefore, expected to significantly enhance the performance of functional DNA origami structures.

In the reconfigurable structure with EtBr binding, second, only twisting reconfiguration is available since EtBr binding occurs uniformly over the structure. Since EtBr binding sites cannot be directed, it is difficult for the structure to be bent with desired curvatures. Therefore, various three-dimensional shapes cannot be

accessed in the dynamic reconfiguration limiting its use in functional nanomachines.

1.4. Thesis overview

In this thesis, I present efforts to improve controllability of twist rate and advance reconfiguration mechanisms through programming mechanical stress (Fig. 1-2). To achieve our goals, we developed two mechanical stress programming strategies using a combination of experiments and computational simulations.

In chapter 2, computational and experimental methods used in the thesis will be described. It will cover modeling and analysis of DNA origami structures in FE and MD simulations, and how to fabricate DNA origami structures through self-assembly and their characterization methods.

In chapter 3, a mechanical stress engineering method, called the configurational design, is presented to finely control a twist rate of the DNA origami structure. It employed the fact that the distance between neighboring crossovers along a certain helix can vary, which is an intrinsic feature of the lattice-based DNA origami structure. Thus, different strain energy can be programmed depending on the position where inserted or deletion BPs are placed. With no change in the number of inserted or deleted BPs, therefore, designing spatial configuration of them can control mechanical strain energies induced enabling fine control on twist rate. To measure twist angles of structures, we took AFM images and analyzed conformation distribution of monomers and inferred twisted angles using a relationship between twist angle and ratio of trans-conformation. Also, FE analysis was employed to reveal a principal design variable in the configurational design as well as to predict

twist angles measured in experiments with high accuracy and to explore numerous design candidates. Combined with a stress relaxing motif, furthermore, the amount of the induced strain energy can be further controlled broadening available design space.

In chapter 4, a mechanical stress engineering method, called the homeomorphic transformation, is demonstrated to reconfigure a closed, circular structure into a supercoiled one with threshold response. It employed that a topological property, the linking number, should be conserved in topologically constrained structures although any deformation occurred. Since the linking number is the sum of the twist and the writhe, any change in either one of them is necessarily accompanied by change in the other. Thus, the local twist induced by EtBr, DNA binding molecules, can be transformed into the global bending deformation reconfiguring a two-dimensional structure into a new class of three-dimensional structural shapes, the supercoiled DNA origami structure. Also, this reconfiguration showed a threshold response, i.e., there was no conformational changes until a critical value of concentration was reached. Through FE analysis on a toy model for the circular DNA origami structure, I found that the conformational change with threshold comes from torsional instability, called Michell's instability. Also, we controlled the reconfigured shapes using control of mechanical properties of the structure through introduction of a locally flexible, structural motif.

Discrete to Semi-continuous twist control	Objective	Simple to Complex reconfiguration
Poor twist rate controllability	Previous problem	Only twist change possible
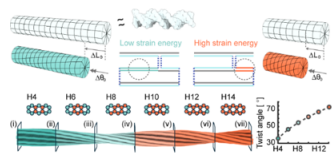	Scheme	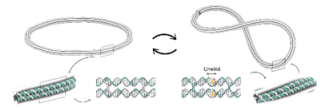
Ch3. Configurational design	Our method	Ch.4 Buckling-induced homeomorphic transformation
Strain energy control	Principle	Coupling of topological properties
Change of the number of BP between crossovers	Geometrical perturbation	Chang of B-DNA geometry
Distribution of Inserted or deleted BP	Stress control	Concentration of binding molecules

Figure 1-2. Comparison of two strategies for mechanical stress engineering for the DNA origami nanostructure.

Chapter 2. Methodology

2.1. Computational modeling and analysis

2.1.1. FE simulation for DNA origami structures

CanDo constructs FE modeling using information on coordinates of BPs, connectivity between BPs and mechanical perturbation introduced by inserted or deleted BPs within structures, which are obtained from parsing caDNAno design files.[41]

A BP was abstracted into a node and two consecutive BPs, corresponding to DNA duplex, were connected by a straight Euler-Bernoulli beam element. In FE model, the DNA duplex was assumed to have the regular B-DNA geometry (diameter of 2.25 nm, axial rise of 0.34 nm and helicity of 10.5 BP/turn) with stretch modulus (S) of 1100 pN, bending rigidity (B) of 230 pN nm^2, and torsional rigidity (C) of 460 pN nm^2. Note that we did not consider any sequence-dependent properties and assumed a nicked DNA duplex to be same with a normal DNA duplex in terms of its geometry and properties. Crossovers are modelled by a beam element that connects two nodes that belong to two adjacent helices, respectively. To consider effect of flexibility of crossover, their mechanical stiffness were defined by multiplying a scale factor (SF) to those of DNA duplex instead of using rigid beams.

When geometrical perturbations due to inserted or deleted BPs, change in geometry of dsDNA or design on the square-lattice exist, structures are not straight. To predict the three dimensional equilibrium shapes considering these geometrical

perturbations, the same procedure described in the literature[42] was used. First, undeformed helices are placed on the lattice without crossovers. Then, they are deformed to connect neighboring helices by crossovers without axial and torsional mismatches and then crossovers are added to couple neighboring helices at crossover locations. After fixing six DOFs at a node and relaxing forces required for deforming helices to remove geometrical mismatches, the final equilibrium shape is computed through a geometrically non-linear FE analysis using the commercial finite element software ADINA.

2.1.2. MD simulation for DNA origami structures

Employing caDNAno, we constructed the initial atomic coordinates of DNA origami structures. They were solvated in a cubic TIP3P[35] water box and electrically neutralized with 20 mM $MgCl_2$. MD simulations were conducted using NAMD[36] with the CHARMM36 force field.[37] Short-range non-bonded potentials including the van der Waals and electrostatic potentials were calculated with a 18 Å cut-off while long range electrostatic interactions were calculated by the Particle Mesh Ewald (PME) method[38] with the grid size of 1 Å. In each system, the potential energy was minimized using the conjugate gradient method. Equilibrium trajectories were simulated under the isobaric-isothermal (NPT) ensemble at 300 K using a Langevin thermostat[36] and 1 bar with Nosé–Hoover Langevin piston.[39] From the MD trajectories, BP step parameters were calculated following the definition in 3DNA[30] that describes the stacking geometry of one BP relative to its neighboring BP.

2.2. Fabrication and characterization

2.2.1. Self-assembly of DNA origami structures.

Using an open source program for design of the lattice-based DNA origami structure, caDNAno, DNA origami structures were designed on the honeycomb lattice with a M13mp18 scaffold strand (7249-NT-long). Sequences of staple strands for structures were obtained from caDNAno and they were synthesized from Bioneer corporation (www.bioneer.co.kr).

A default folding mixture consists of 10 (or 20) nM concentration of scaffold DNA (New England Biolabs or GUILD), 100 nM of each staple strands (Bioneer), 1×TAE buffer (40 mM Tris-acetate and 1 mM EDTA) and 20 mM of $MgCl_2$ (Sigma-Aldrich). When a higher concentration is required, more scaffold strand is used for self-assembly.

The annealing process for self-assembly of DNA strands was performed on a temperature gradient from 80℃ to 65℃ by -0.25℃/min and 65℃ to 45℃ by -1℃/hr in a thermocycler (T100, Bio-Rad). Folded structures were stored at -4℃ in a refrigerator.

A concentration of folded structures was measured using a UV spectrophotometer, Nanodrop One (Thermo Fisher Scientific). If required, excessive staple strands were removed through five buffer exchange procedures[19] at 5 krcf during 8 min and concentration of structures were adjusted using the same buffer used in folding (1xTAE and 20 mM of $MgCl_2$).

2.2.2. Agarose gel electrophoresis.

Annealed samples of DNA origami structures were electrophoresed using 1.5% agarose gel containing 0.5xTBE (45 mM Tris-borate and 1 mM EDTA, Sigma-Aldrich), 12 mM of $MgCl_2$, and in 0.5 µl/ml of ethidium bromide (EtBr, Noble Bioscience Inc.). For each sample line, a sample of 15 µl was added, which consists of 3 µl of 6X-DNA gel loading dye (Thermo Fisher) and 12 µl of DNA structures. Electrophoresis was performed for 1.5 hours at 75 V bias voltage (~ 3.7 V/cm) in an ice-water cooled chamber (i-Myrun, Cosmo Bio CO. LTD.). Gel imaging was performed using GelDoc XR+ device and Image Lab v5.1 program (Bio-Rad).

.

2.2.3. AFM imaging

Annealed sample was diluted by folding solution (1×TAE and 20 mM $MgCl_2$) prior to deposition in order to control the number of monomers on the substrate. Generally, 0.5 to 1 μM of annealed structures is appropriate for image analysis. 20 μl of diluted sample was then deposited and incubated on a freshly cleaved mica substrate (highest grade V1 AFM Mica, Ted-Pella Inc.) for 5 minutes. We washed the substrate with DI water and gently dried it using N_2 gun (< 0.1 kgf/cm^2). If the number of monomer in images is small, a longer deposition and a higher concentration of sample can be used.

AFM images were taken by NX10 (Park Systems) using non-contact mode in SmartScan software. A PPP-NCHR probe with spring constant of 42 N/m was used in the measurements (Nanosensors). Images were flattened with linear and quadratic order using XEI 4.1.0 program (Park Systems). Single particle images of DNA origami structures were extracted from AFM images using the MATLAB script provided in the literature[16] and classification of single particles was manually done.

2.2.4. TEM imaging

After removing excessive staples annealed samples by the buffer exchange[19], the sample was diluted to 1 μM monomer solution. Formvar/Carbon TEM grid (400 mesh copper, Ted-Pella Inc.) were plasma treated for 20 sec with 15 mA glow discharge. A 3 μL of diluted samples were applied on the TEM grid and incubated for 3 min. The remaining solution was washed by DI water and then absorbed by a filter paper. Next, 20 μL of a 2% uranyl-formate solution was applied. Samples were incubated for 40 sec for negative staining of the DNA origami structures and then staining solutions were removed by a filter paper. After dried for 10min, samples were scanned on Talos L120C (Thermo Fisher) operated at 120 kV.

Chapter 3. Mechanical stress engineering for fine shape control

3.1. Limitation in the design of twisted structures

Most non-straight DNA origami structures have been designed by applying the concept of BP insertion and deletion to the straight, reference structure[49]. They basically serve as mechanical perturbation to the reference structure making it bent and twisted to minimize the geometric misalignment of BPs at crossover positions. The curvature and twist rate can be easily modulated by just varying the number of these BPs introduced. While this design approach is quite simple and effective, it has an intrinsic limitation in that only natural numbers of BP insertion and deletion can be used resulting in discrete values of curvature and twist rate achievable. Alternative methods were proposed for curved structures such as compliant[34] and modular[35] design approaches, but a design method for precise twist control has rarely been found. While it is possible to tune the twist rate of entire structure homogeneously by changing the DNA helicity through, for example, binding DNA intercalators[53] and UV lights[51], these methods cannot be used to control the twist rate locally and hence to realize its spatial variation.

Here, we present a design strategy for twisted DNA origami structures considering not only the number of BP insertion and deletion but also their arrangement within the structure. It utilizes the fact that the strain energy induced by inserted/deleted BPs differs depending on their location even if the same number of

BPs is used. We can program various spatial distributions of this strain energy by the configurational design of insertions and deletions enabling a fine control over the twist rate of DNA origami structures. To demonstrate, we consider a 6HB reference structure on the honeycomb lattice and its torsional variants systematically designed by the proposed method. In this case, we could achieve the twist rate of a 21-BP-long unit block ranging from 15.0º to 25.7º with the mean increment of 1.8º by manipulating the arrangement of six inserted BPs within the unit block where each helix has a single insertion only. Molecular dynamics (MD) simulations revealed that the induced strain energies were mainly relaxed by the deformation of Holliday junctions (HJs) rather than that of BP itself and the deformed conformations of HJ are dependent on the configuration of mechanical perturbations. Even broader twist control with fine tunability was also shown to be possible by introducing gaps, short unpaired NTs, at nick positions that relax the strain energy induced by mechanical perturbation *via* insertions and deletions. Our design approach is expected to significantly expand the feasible design space of twisted DNA origami structures enabling us to harness the superior physical properties of twisted architectures observed in many natural and synthetic materials[21, 58-62].

3.2. Configurational design approach

In lattice-based DNA origami structures, the crossover spacing varies along a helix in general. For example, for a straight structure designed on a honeycomb lattice where each helix has three adjacent helices to be connected, crossovers exist every 7 BPs in inner helices when all possible crossovers form excluding relatively sparse scaffold crossovers. However, the outermost helices have the crossover spacing alternating 7 BPs and 14 BPs because only two neighboring helices are available for them. Particularly for 6HB structures with a closed cross-section, the crossover spacing of every helix alternates in the same way (Fig. 3-1A). This variable crossover spacing makes, in fact, the location of inserted/deleted BPs important in structural design. Given the geometric mismatch determined by the number of inserted/deleted BPs, the strain energy induced by them is dependent on the stiffness of a helix segment where they locate, which is inversely proportional to its reference length or the crossover spacing (Fig. 3-1B). As a result, the strain energy due to insertions or deletions in a helix segment of 7-BP crossover spacing is approximately two times higher than that when introduced to a 14-BP region. Thus, we can achieve various spatial distributions of the strain energy along the helix and across the cross-section by programming the location of inserted/deleted BPs. This offers a versatile way of building twisted DNA origami structures with a broad range of twist rates as the configurational design space expands with the number of helices and inserted/deleted BPs even with these two positional options for each insertion or deletion.

We tested this design principle computationally using the finite element (FE)

model for DNA origami, CanDo[41-43], which can predict its equilibrium shape. Two twisted 6HB structures were designed by incorporating insertions into the reference structure consisting of seven 21-BP-long unit blocks (Fig. 3-1C). Only one insertion was allowed on either 7-BP or 14-BP helix segment in each helix of a unit block (six insertions in total per unit block). We devised two representative configurations of inserted BPs: the minimum-strain-energy configuration where all insertions were located in the 14-BP helix segments and the maximum-strain-energy configuration where they populate the 7-BP helix segments only.

Twist angles predicted by CanDo analysis for each configuration were 84.0º and 165.6º (Appendix. A1), respectively, demonstrating the potential of the proposed design approach. Since the variable crossover distance is an inherent structural feature of DNA origami structure, our method can be easily applied to modulate the twist angle of any other structure with an arbitrary cross-sectional shape designed on any lattice type. To illustrate, we additionally designed seven reference structures (four on a honeycomb lattice and three on a square lattice) with two representative insertion configurations for each structure (Fig. 3-1D). The strain-energy-based configurational design approach worked pretty well as confirmed by CanDo analysis even though each helix of a structure had a different crossover spacing depending on the lattice type, the location of a helix on the lattice, and the connectivity among neighboring helices.

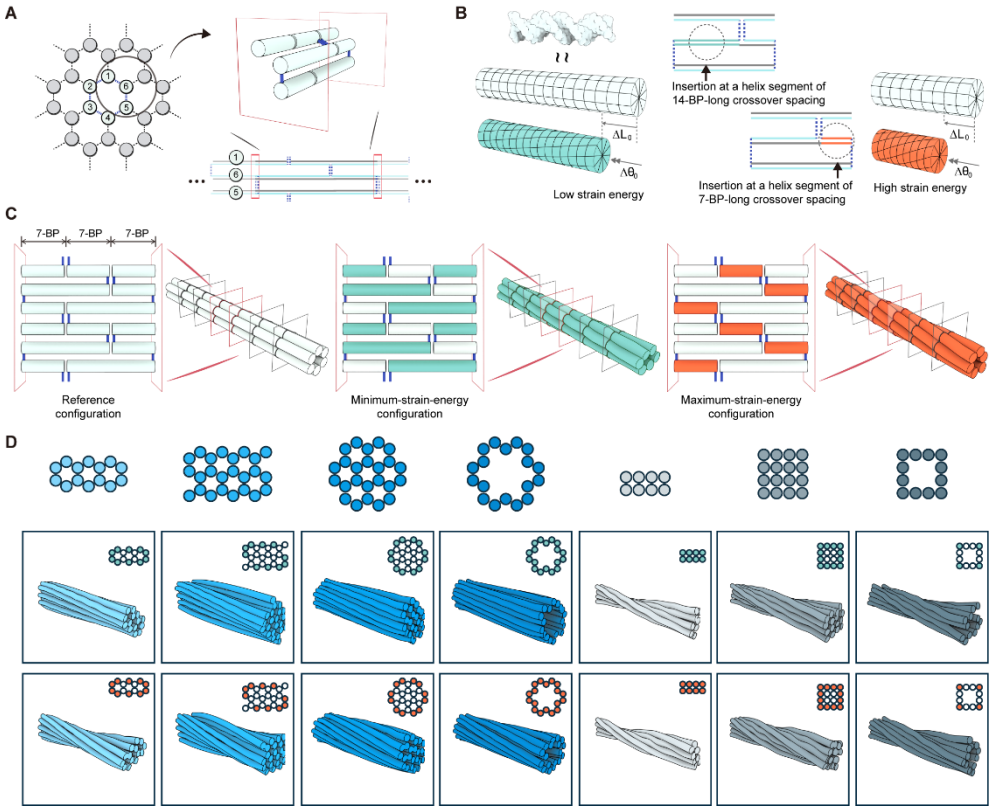

Figure 3-1. Concept of the configurational design of mechanical perturbation. (**A**) Variable crossover spacing of 6HB on the honeycomb lattice. DNA helices are represented using cylinders and crossovers are denoted using blue cylinders or lines. (**B**) Insertion-induced strain energy. For the same displacements required for alignment of BPs at crossovers, different strain energies are induced depending on the crossover spacing of a helix segment where BPs are inserted. ΔL0 and Δθ0 represent axial and torsional displacements necessary for alignment, respectively. Green and red colors indicate that insertions are located in a helix segment of 14- and 7-BP-long crossover spacing, respectively. (**C**) Examples of insertion configuration. No inserted BPs exist in the reference configuration. All the insertions are located in 14-BP-long helix segments for the minimum-strain-energy

configuration while in 7-BP-long ones for the maximum-strain-energy configuration. (**D**) Applications of the configurational design approach to various cross-sectional shapes. Middle and bottom rows represent the minimum- and maximum-strain-energy configurations, respectively. Inset figures show the insertion configurations where green and red circles denote the helices with low- and high-strain-energy insertions, respectively. Twisted shapes were predicted by CanDo.

3.3. Twist angle variation

To investigate this idea for twist control systematically and quantitatively, we designed a straight, reference DNA origami structure divided into two parts: variable body (VB) and fixed body (FB) (Fig. 3-2A). Twenty unit blocks consisting of six 21-BP-long helices comprise VB whose twist rate can be controlled by insertions or deletions to build a right-handed or left-handed twisted structure, respectively. At the ends of VB, two straight FB parts are attached. Each part has the flag region consisting of ten 63-BP-long helices pleated into a single layer in addition to the 6HB core. The flags of FB are deliberately added to the structure in order to distinguish two conformational states of the twisted structure when deposited on a mica surface by atomic force microscopy (AFM) imaging[53]. Two long single strand DNA (ssDNA) loops exist at the interfaces between VB and FB to feed additional bases or accommodate remaining ones required for any change in VB keeping the sequences of DNA strands in FB unchanged.

Torsional variants of the reference structure were designed and constructed by systematically varying the number of twisted unit blocks in VB and their twist rate (Fig. 3-2A and 3-3 and Table 3-1 to 3-2) determining the total twist angle of these structures. We allowed only a single BP insertion or deletion to each helix per unit block, referred to as the insertion or deletion block, respectively. Two representative configurations of inserted or deleted BPs were devised by putting all of them to the 14-BP helix segments or to the 7-BP helix segments. These two configurations are denoted by H0 and H6, respectively, where H indicates the helix segment of high-strain-energy (or 7-BP crossover spacing) and the number next to it

represents the total number of insertions or deletions located in this segment. Hence, unit blocks in H0 configuration have insertions or deletions only in the 14-BP helix segments leading to the smallest twist rate while those in H6 configuration exhibit the largest one.

These structures can have two distinct conformations when deposited on a mica surface that can be easily identified by relative position of two flags of successfully folded monomers in AFM images. Two flags can appear on the same or opposite side of the structure referred to here as cis- or trans-conformation[53], respectively (Fig. 3-2B). Both conformations would be observed for any designed structure due to probabilistic nature of deposition, but their ratio would differ depending on the twist angle of the structure. Cis-conformation would dominate if the twist angle is closer to 0º while the structure in trans-conformation would be more populated if it is designed to be twisted by near 180º.

We measured the trans-conformation ratio (TR) of successfully folded monomers from AFM images to estimate the twist angle (Fig. 3-4 to 3-12 and Table 3-3). Note that TR for the straight structure is non-zero as trans-conformation is also possible for it mainly due to thermal fluctuation of its twist angle in solution[53]. TR increased naturally with the number of insertion or deletion blocks in both H0 and H6 configurations until it reached the peak corresponding to the twist angle of 180º (Fig. 3-2C). Then, it began to decrease as the twist angle became larger than 180º. We could observe a significantly higher rate of change in TR when H6 configuration was used for unit blocks, confirming the effect of configurational design of inserted/deleted BPs on the twist rate of a unit block. Slightly lower TR values were obtained when deletion blocks were used probably because the structure with

deletion blocks would be shorter than that with insertion blocks making it stiffer in torsion. Measured TR values nicely showed sinusoidal profiles with respect to the number of blocks, except for unexpectedly low TR observed when 14 insertion blocks in H0 configuration were used due to unidentified reasons. We quantified the mean twist rate of insertions block in both configurations from the measured TR curves. Here, we assumed that the twist angle of the structure increases linearly with the number of insertion blocks, the minimum and maximum TR values correspond to the twist angles of 0º and 180º, respectively, and TR curves are symmetric about their peak. Since the peak TR points appeared at 12 insertion blocks for H0 configuration and 7 blocks for H6, the mean twist rates of 15.0º and 25.7º were estimated for H0 and H6 configurations, respectively, revealing the power of configurational design.

We calculated the twist angles of folded structures using CanDo and converted them into TR values using a simple geometrical model[53] (Appendix A2). However, CanDo underestimated the twist angle compared to experiments. We conjectured that this discrepancy would come from a simplified mechanical model for crossovers assumed as rigid beams in CanDo[41-42] while Holliday junctions (HJs), the antiparallel double crossovers, have been known to be flexible[63]. Sensitivity analysis[30] for the crossover properties on the twist rate revealed that their effect becomes non-negligible if HJs are as flexible as the DNA duplex and, in particular, their bending stiffness has the highest influence on the twist rate of the structure (Fig. 3-13). Hence, we developed a flexible crossover model whose bending stiffness was chosen such that the predicted twist angle of the structure with 12 insertion blocks in H0 configuration became 180º as expected from the experiments (Table 3-4).

We also confirmed that the twist rates of sixty-helix bundles predicted by the flexible crossover model were well matched with the experimental ones reported previously (Fig. 3-14)[49]. Then, we calculated the twist angles of all the other structures using CanDo with the flexible crossover model. Converted TR values agreed pretty well with the experimental ones for structures design with both H0 and H6 unit blocks.

200-ns-long MD simulations for much shorter 6HB structures consisting of three unit blocks (Fig. 3-15A) also confirmed the difference between H0 and H6 configurations (Fig. 3-15B and 3-16). Twist angles corresponding to two unit blocks were measured from the MD snapshots of last 80 ns to reduce the effect of unconstrained flanking helices, resulting in mean twist angles of 36.0º and 59.3º for H0 and H6 configurations, respectively. While MD simulations slightly overestimated the twist angles compared to the experimental values (30.0º and 51.4º), they clearly showed the substantial effect of configurational design. More quantitative analysis of HJ conformations revealed the structural difference of two insertion configurations at the molecular level (Fig. 3-15C). Here, we employed the conformational parameters for HJs used in the analysis of the pointer-like DNA origami structure[63] using MD trajectories every 4 ps during the last 80 ns for two unit blocks to reduce the effects of unconstrained helices at both ends. While both twisted structures commonly showed left-handed HJ on average as indicated in their leg-to-leg inclination distribution, HJ legs in H6 configuration were less bent away from the plane than those in H0 configuration. The decrease in local bending at HJs might explain why it showed weaker undulation of individual helices (Fig. 3-16). This is probably because 7-BP helix segments are stiffer than 14-BP ones, and

therefore HJ legs can be bent less when BPs are inserted into 7-BP segments. In contrast, no significant changes in BP step parameters[64] were observed for twisted structures (Fig. 3-17 and Table 3-5). Hence, it is suggested that the bundle twist is mainly achieved by conformational changes of HJs.

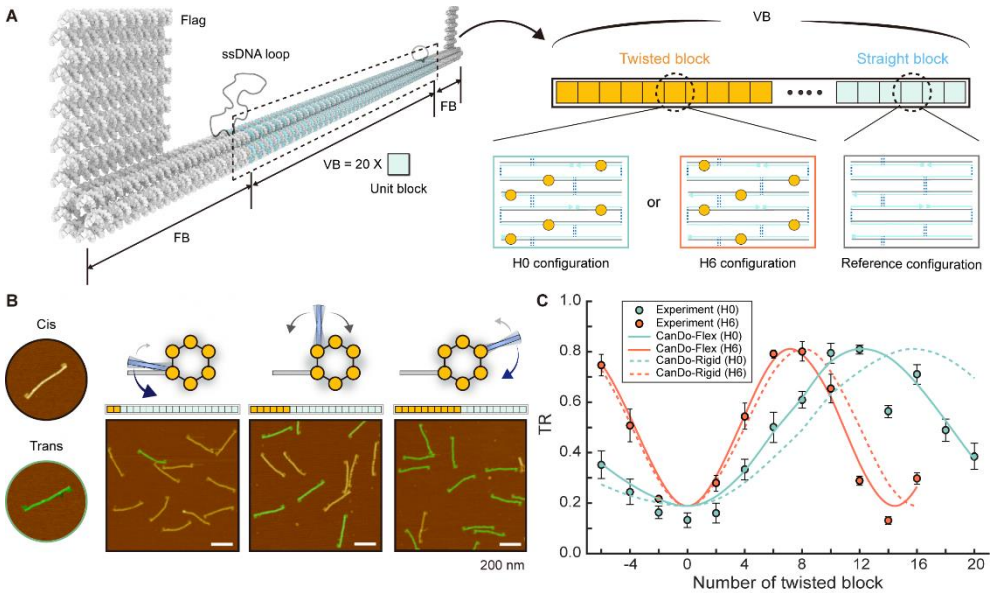

Figure 3-2. Twist angle variation for 6HB DNA origami structures. (**A**) Reference 6HB design. Cyan and gray colors represent VB and FB, respectively. In VB, cyan and yellow squares denote the straight and twisted blocks whose numbers and insertion or deletion configuration can be varied. (**B**) Representative AFM images of cis- and trans-conformations of 6HB and three representative twist angles, number of twist blocks used, and the corresponding AFM images. Monomers in the trans-conformation were colored in green. The arrows indicate the direction in which the blue flag of 6HB would rotate when the structure is deposited on a mica surface. A thicker arrow represents the direction of higher probability. (**C**) TR values measured experimentally and predicted by CanDo analysis. Circles represent TR values by counting the number of cis- and trans-conformers in all AFM images. Solid and dashed lines show TR variations with respect to the number of twisted blocks predicted by CanDo analysis with flexible and rigid crossover models, respectively. Positive numbers of twisted block indicate the number of insertion blocks while

negative ones denote that of deletion blocks.

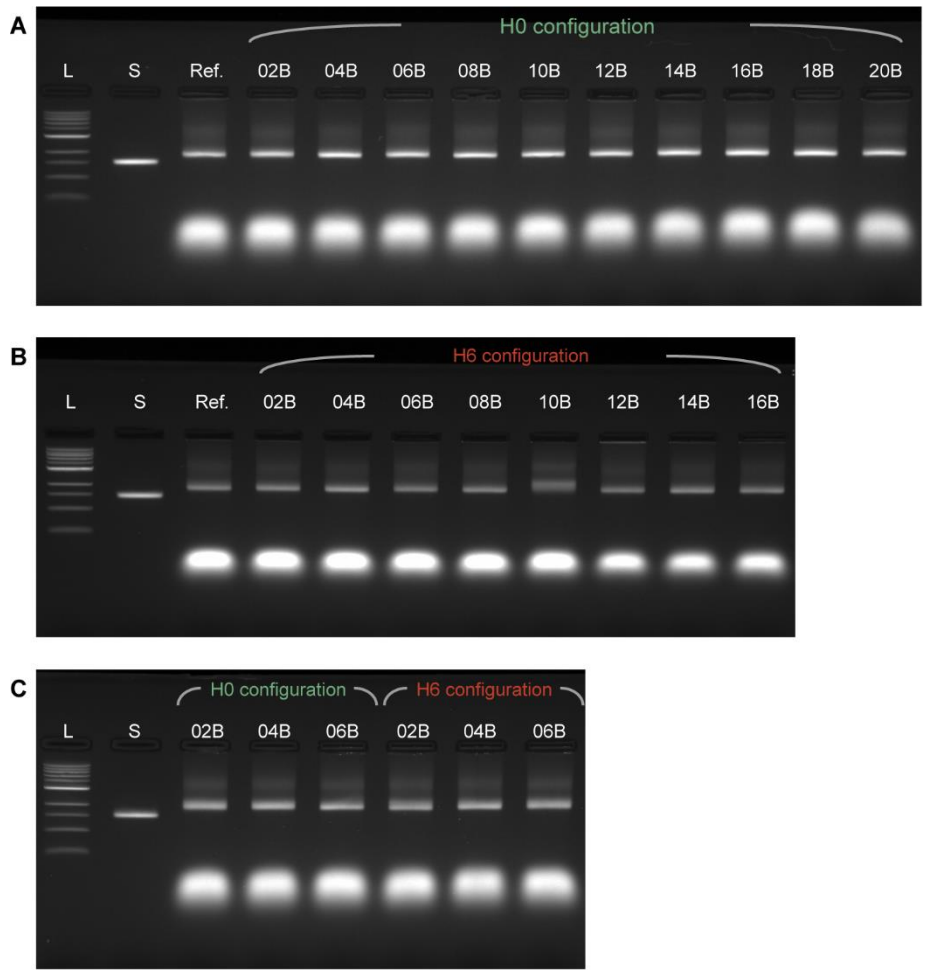

Figure 3-3. **Agarose gel electrophoresis results of all structures shown in Fig. 3-2C.** (**A**) 6HB structures in the reference and the H0 configuration with different numbers of insertion blocks in VB. (**B**) 6HB structures in the reference and the H6 configuration with different numbers of insertion blocks in VB. (**C**) 6HB structures with different numbers of deletions blocks for both H0 and H6 configurations. L: 1kb DNA ladder and S: Scaffold strand.

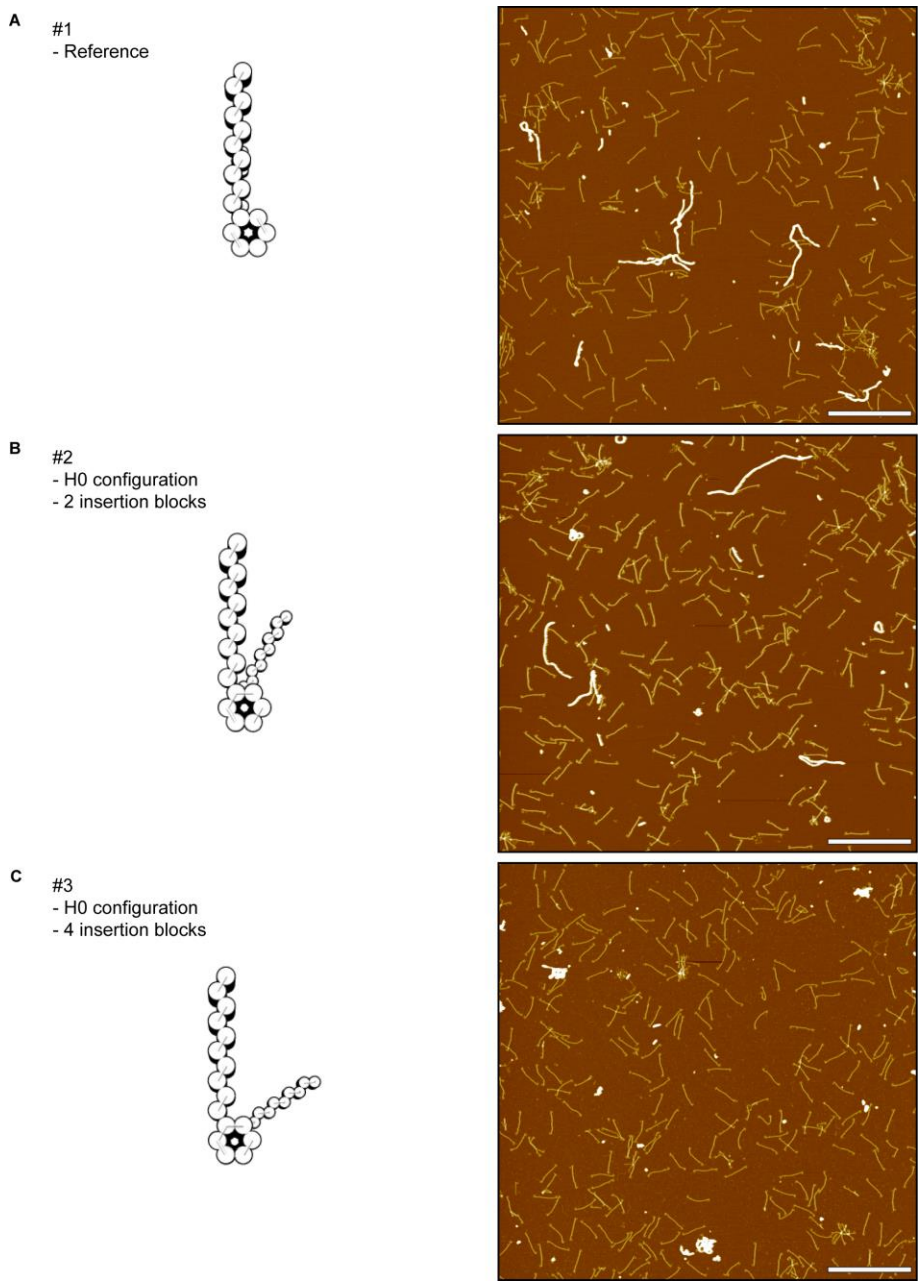

Figure 3-4. **The CanDo analysis with flexible crossover model (left) and the representative AFM images (right) of 6HB structures (#1 to #3) shown in Fig. 3-2C.** Scale bars: 1 μm.

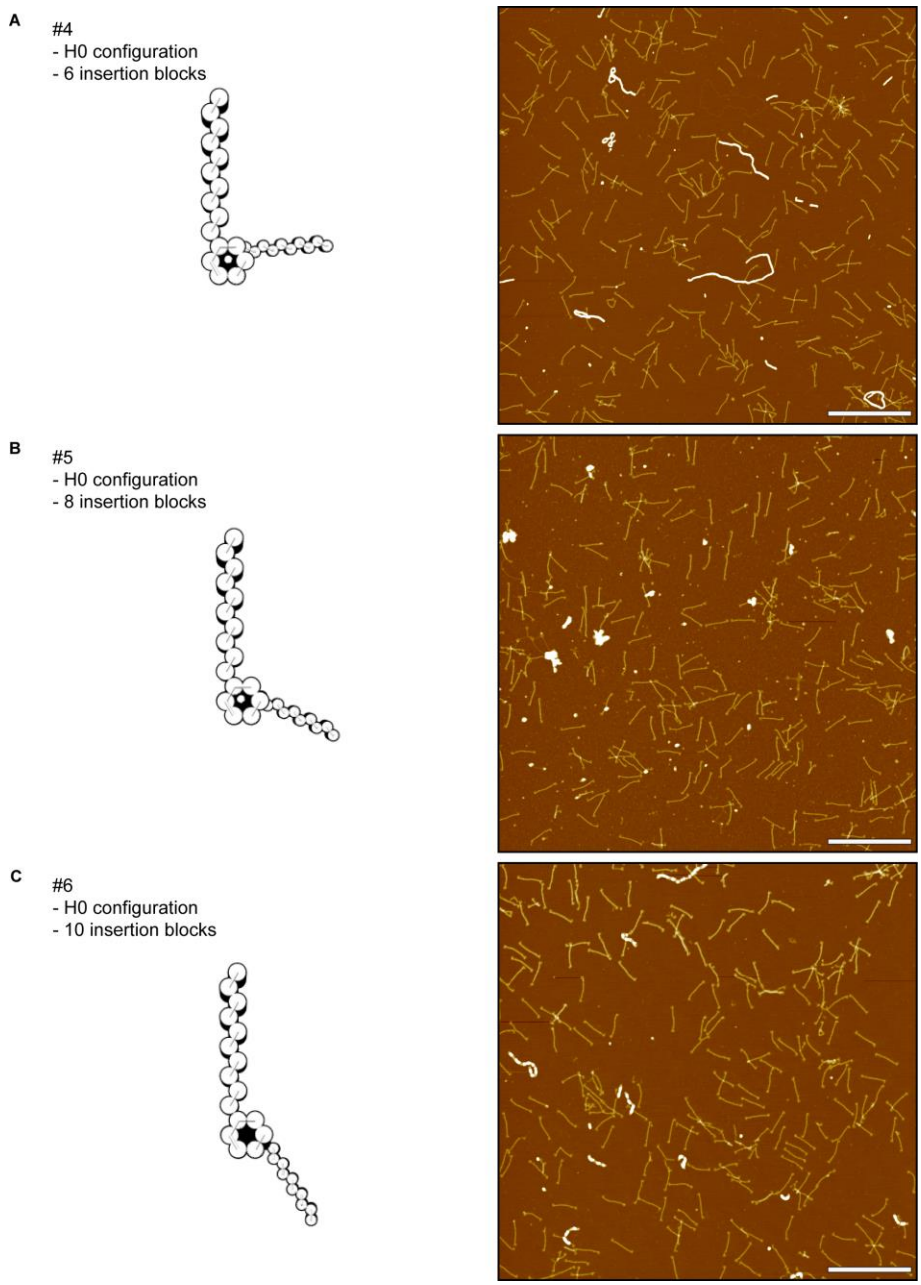

Figure 3-5. **The CanDo analysis with flexible crossover model (left) and the representative AFM images (right) of 6HB structures (#4 to #6) shown in Fig. 3-2C.** Scale bars: 1 μm.

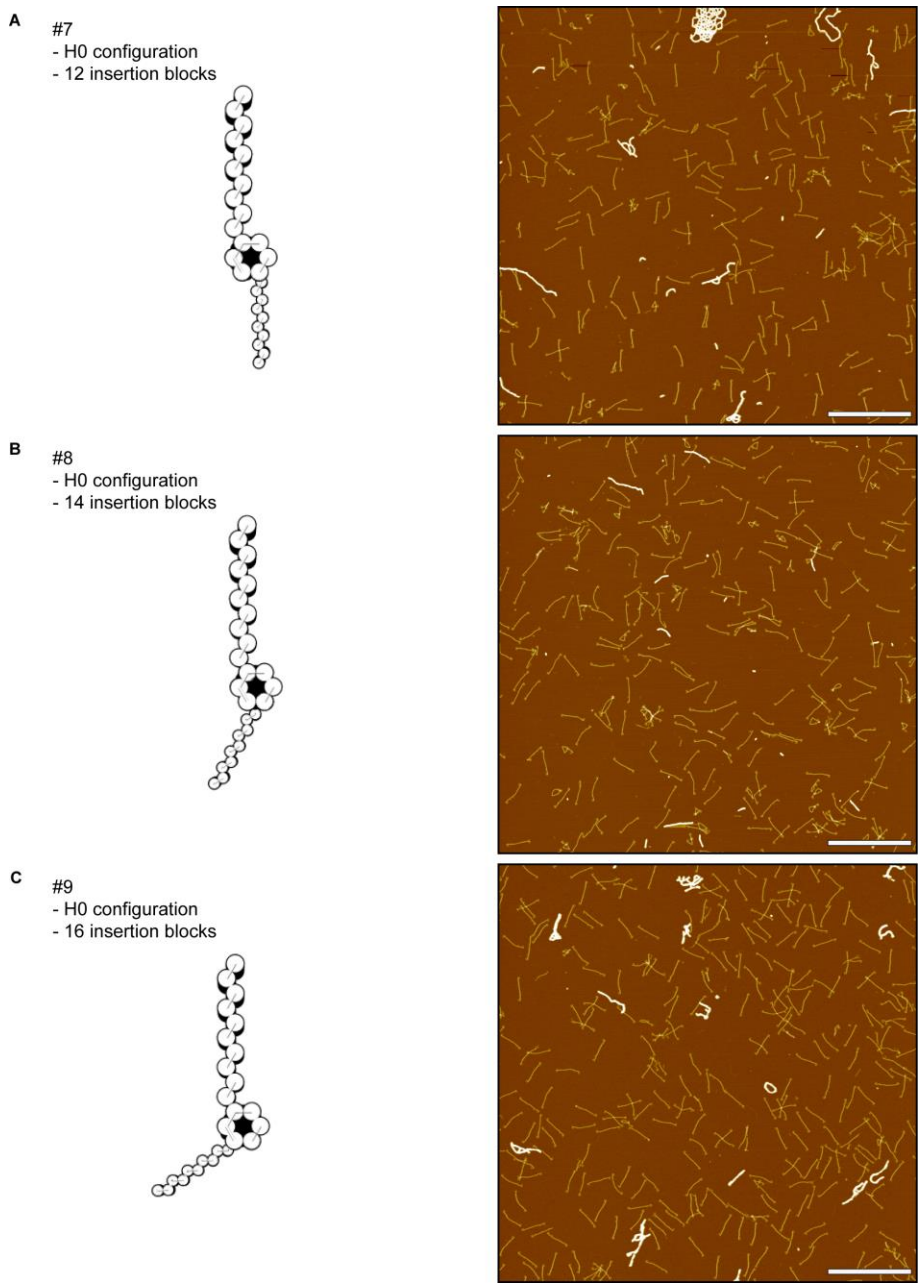

Figure 3-6. **The CanDo analysis with flexible crossover model (left) and the representative AFM images (right) of 6HB structures (#7 to #9) shown in Fig. 3-2C.** Scale bars: 1 μm.

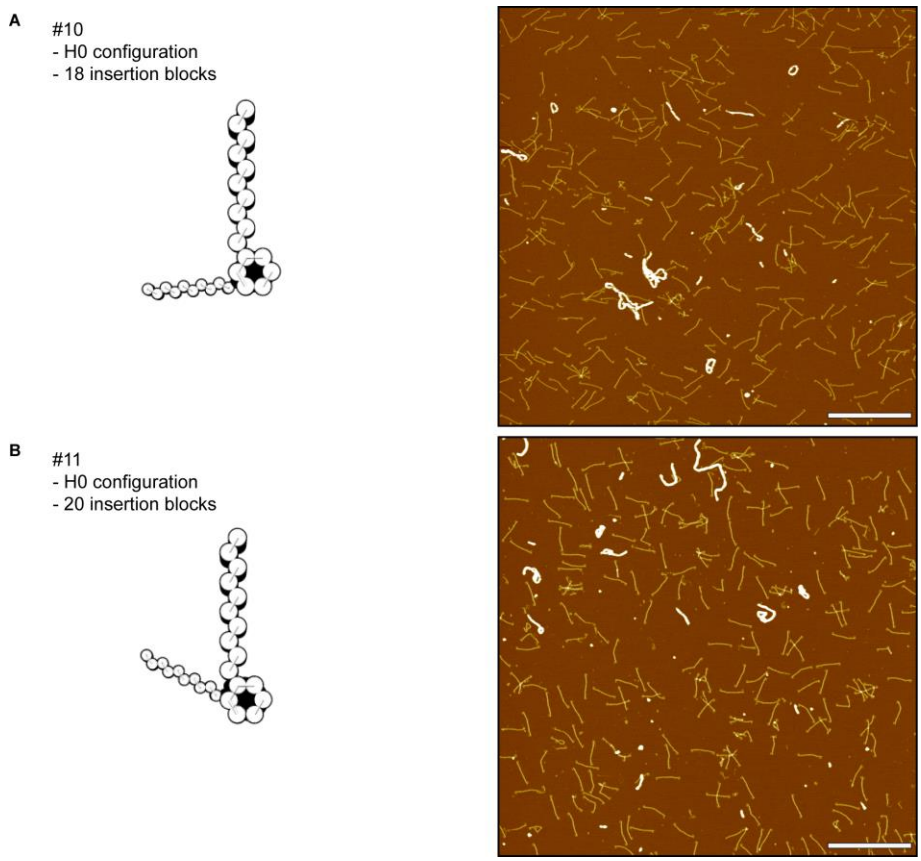

Figure 3-7. **The CanDo analysis with flexible crossover model (left) and the representative AFM images (right) of 6HB structures (#10 to #11) shown in Fig. 3-2C.** Scale bars: 1 μm.

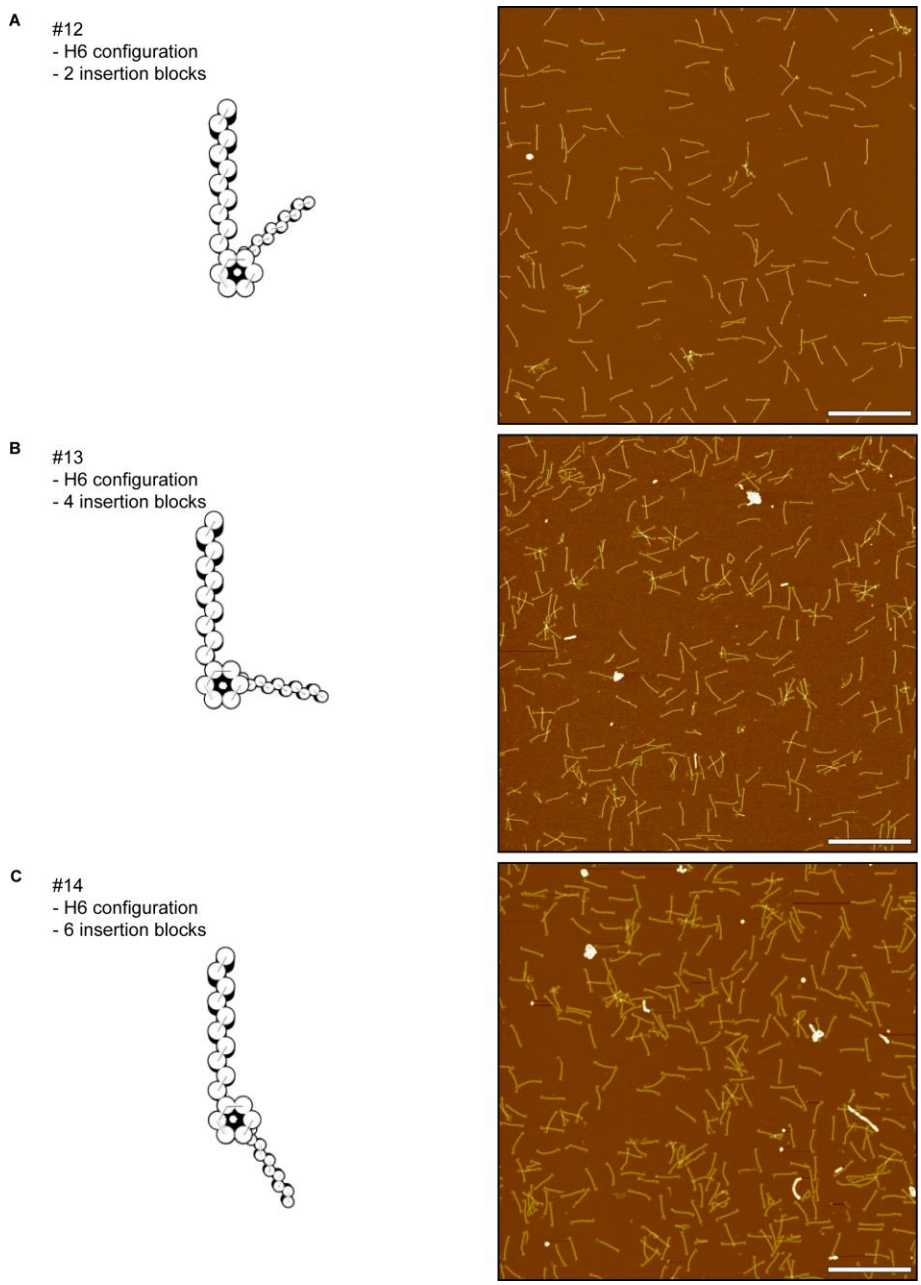

Figure 3-8. **The CanDo analysis with flexible crossover model (left) and the representative AFM images (right) of 6HB structures (#12 to #14) shown in Fig. 3-2C.** Scale bars: 1 μm.

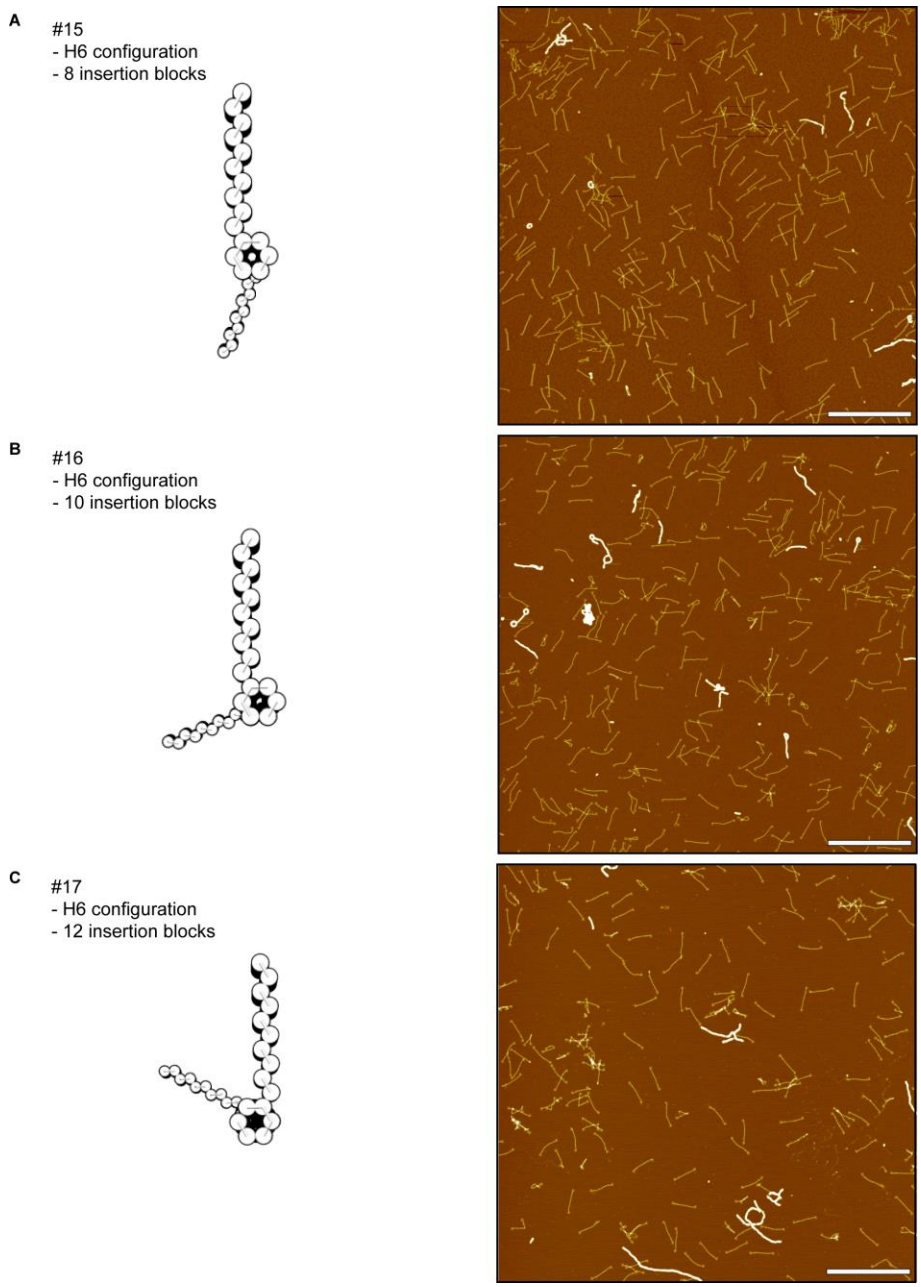

Figure 3-9. **The CanDo analysis with flexible crossover model (left) and the representative AFM images (right) of 6HB structures (#15 to #17) shown in Fig. 3-2C.** Scale bars: 1 μm.

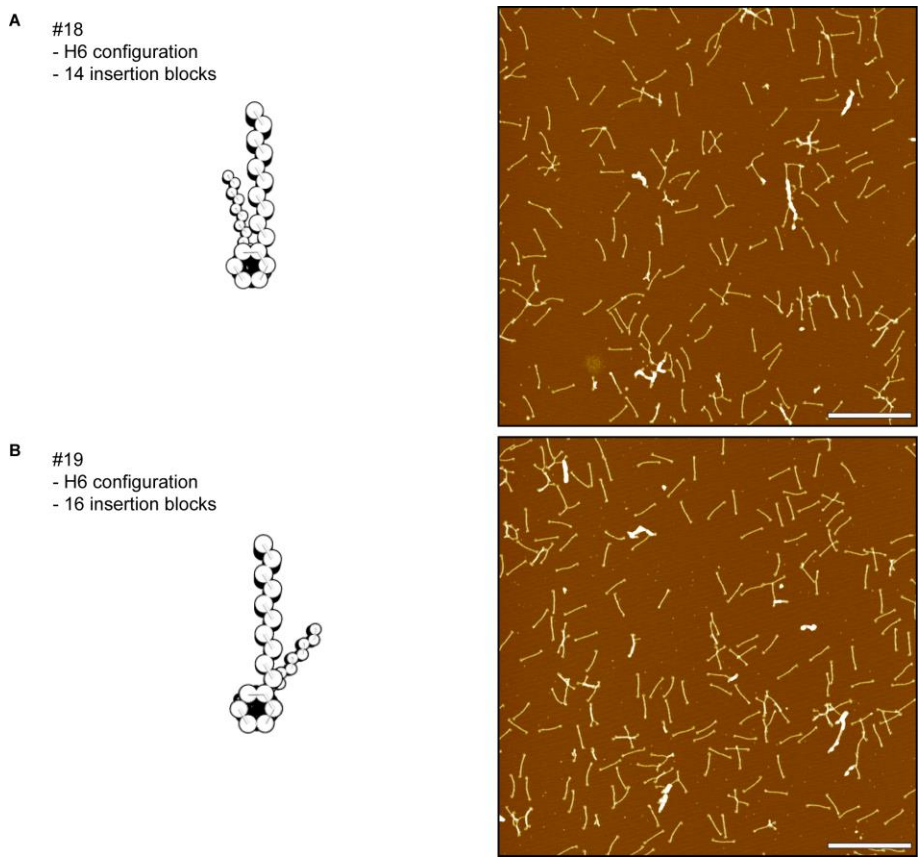

Figure 3-10. **The CanDo analysis with flexible crossover model (left) and the representative AFM images (right) of 6HB structures (#18 to #19) shown in Fig. 3-2C.** Scale bars: 1 μm.

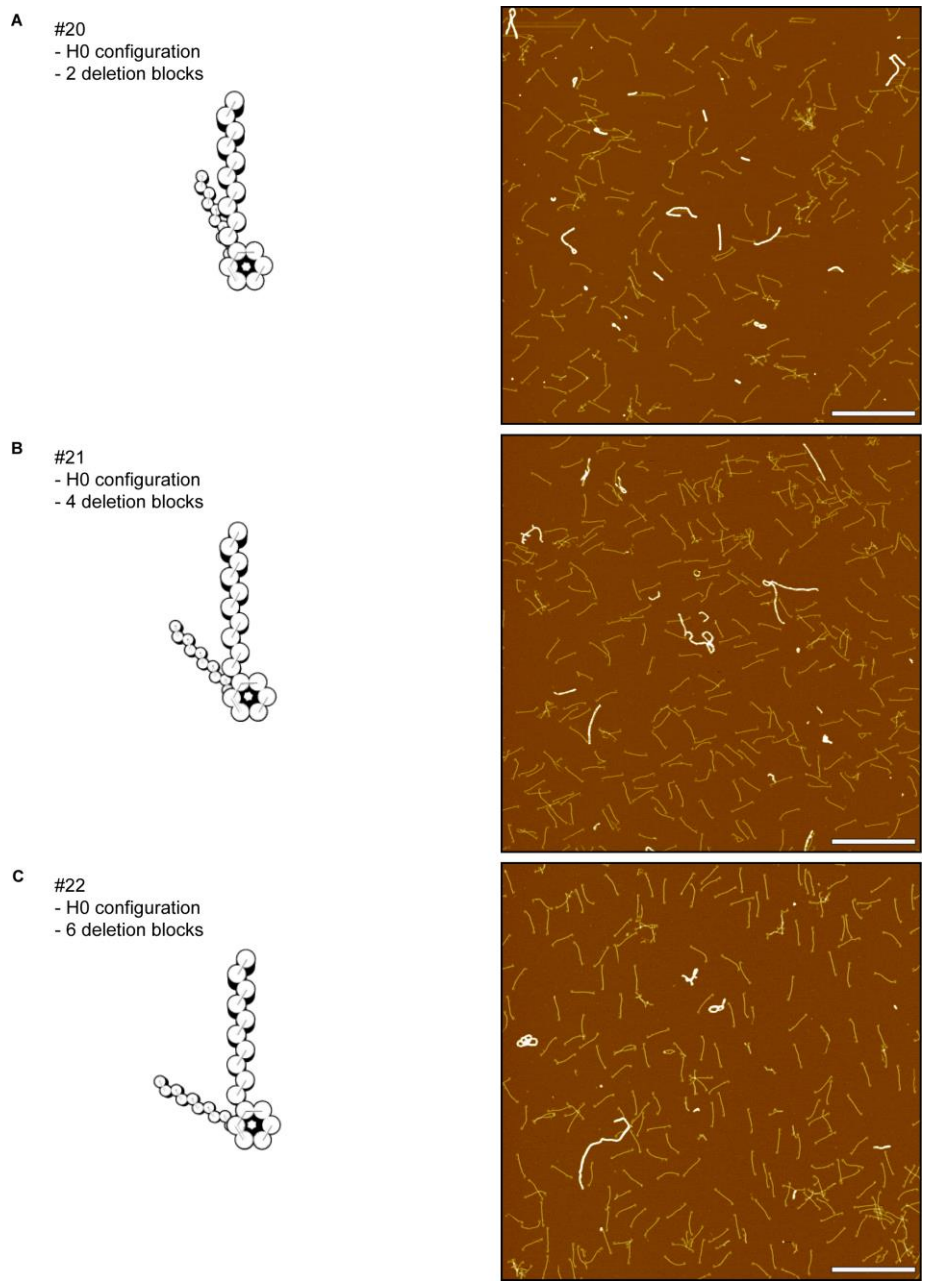

Figure 3-11. **The CanDo analysis with flexible crossover model (left) and the representative AFM images (right) of 6HB structures (#20 to #22) shown in Fig. 3-2C.** Scale bars: 1 μm.

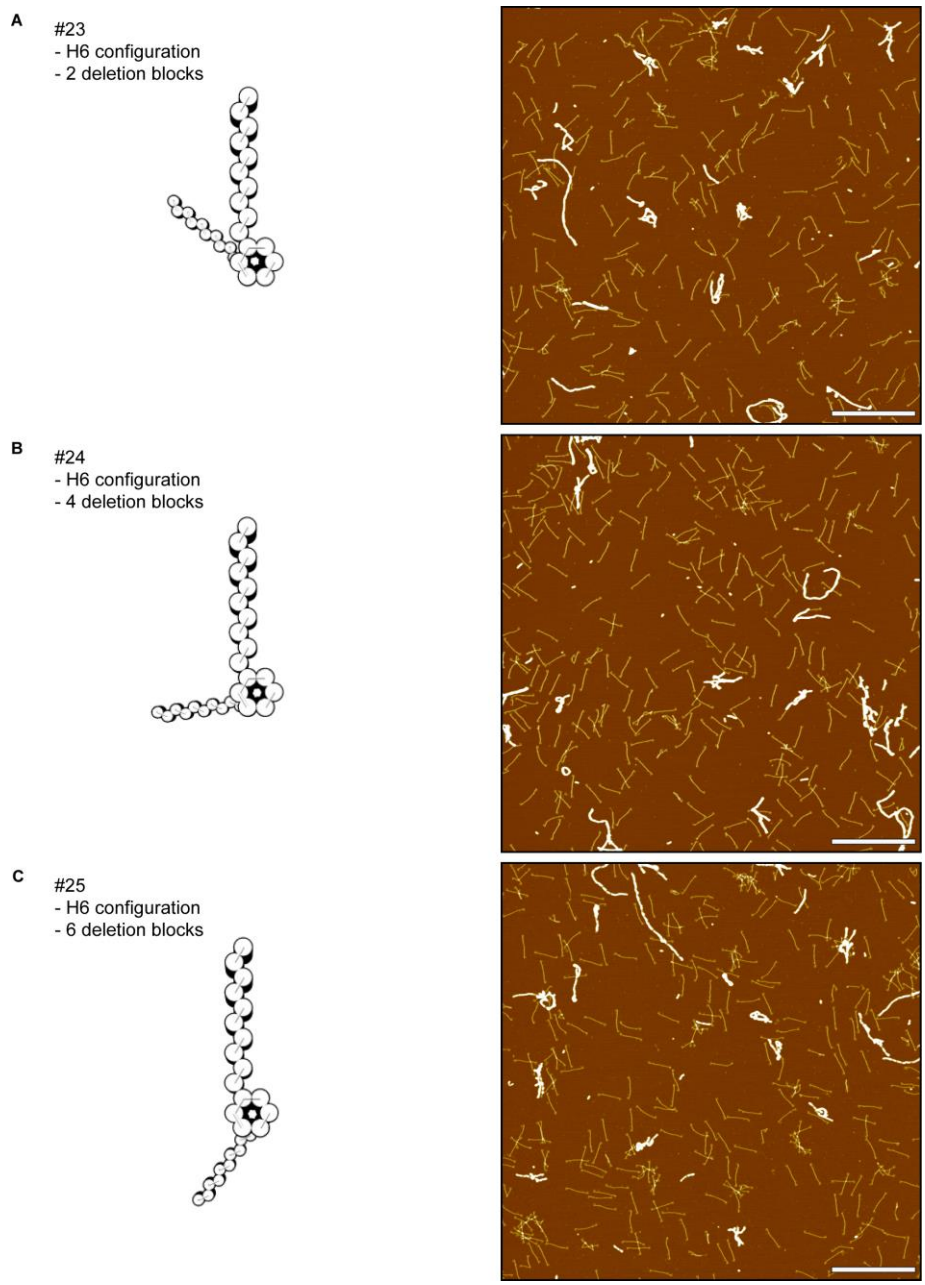

Figure 3-12. The CanDo analysis with flexible crossover model (left) and the representative AFM images (right) of 6HB structures (#23 to #25) shown in Fig. 3-2C. Scale bars: 1 μm.

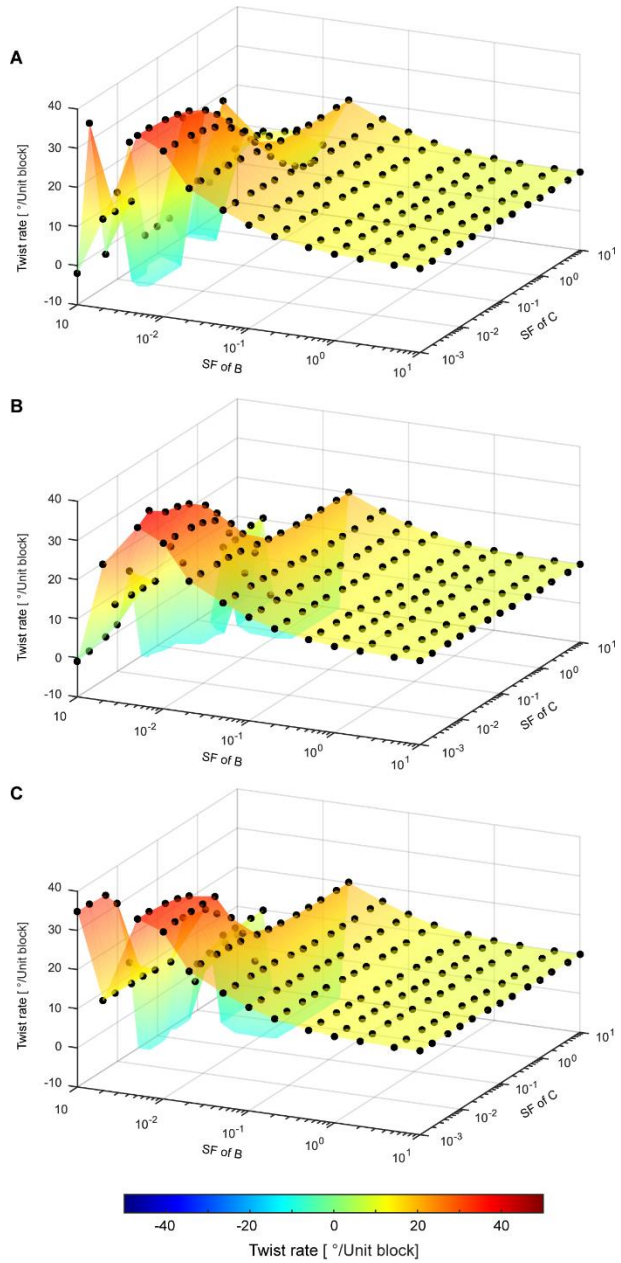

Figure 3-13. **The sensitivity analysis for crossover properties on the twist rate.** For the H0 insertion configuration, the sensitivity analysis of crossover model used in CanDo analysis on the twist rate varying mechanical properties of crossovers. For the axial stiffness, we tested three different scale factors (SF) (**A**) of 0.1, (**B**) 1, and (**C**) 10.

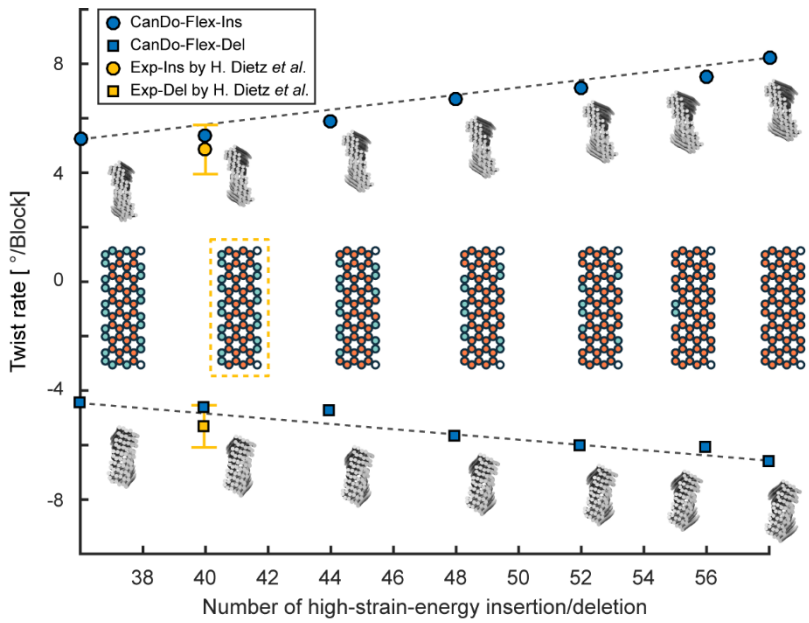

Figure 3-14. Twist rate of sixty-helix-bundle (60HB). We applied our design approach into 60HB provided by H. Dietz *el al*.[49] For 60HB with right-handed twist, we designed six different 60HBs as well as the one in the literature by just varying position of inserted BPs within a 21-BP-long unit block without change of the total number of them within the unit block and predicted their twist rates using the refined CanDo. Twist rates of 60HB were varied from 5.23º to 8.22º with a mean increment of 0.5º. More fine control would be achievable through a smaller variation in number of high-strain-energy insertion. In the same way, various 60HBs with left-handed twist were designed and their twist rate (-6.57º ~ -4.45º) were predicted. Also, we confirmed that CanDo with the flexible crossover model can predict similar twist rates to experimental ones in the other cross-section as well as 6HB.

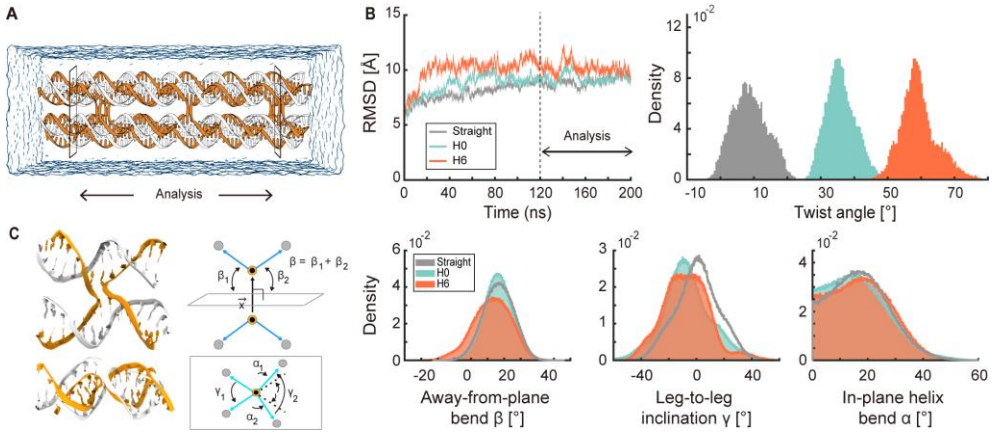

Figure 3-15. MD simulations for 6HB models. (**A**) Atomistic 6HB model for MD simulations. (**B**) Root-mean-square deviation (RMSD) histories (left) and the twist angle distributions (right). Mean twist angles of the reference, H0, and H6 configurations are 8.8º, 36.0º, and 59.3º, respectively. (**C**) HJ conformational parameters[28] from MD trajectories. Yellow circles are midpoints of two BPs in each helix at HJ while gray circles indicate BPs, 2-BP away from HJ. Blue arrows connecting these circles represent HJ legs. Cyan arrows are obtained by projecting HJ legs onto a plane, which is normal to an auxiliary vector ($\vec{x}$).

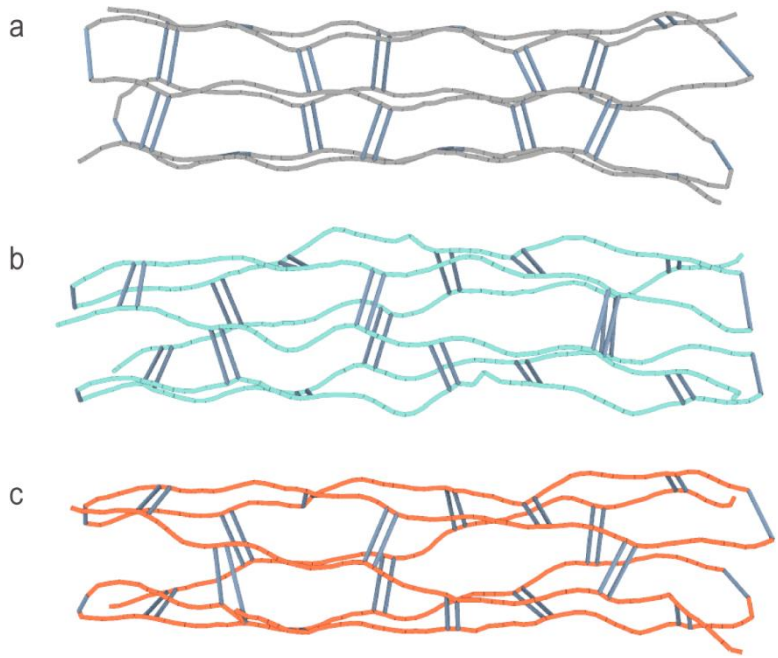

Figure 3-16. Representation of mean configurations for short 6HB structures obtained from molecular dynamic (MD) simulations. The reference (top), the H0 (middle) and the H6 configuration (bottom) obtained from trajectories during the last 80 ns of all-atom MD simulations. Wires represent connections between neighboring centers of BPs. Gray, green and red lines correspond to DNA duplex and blue lines display crossovers.

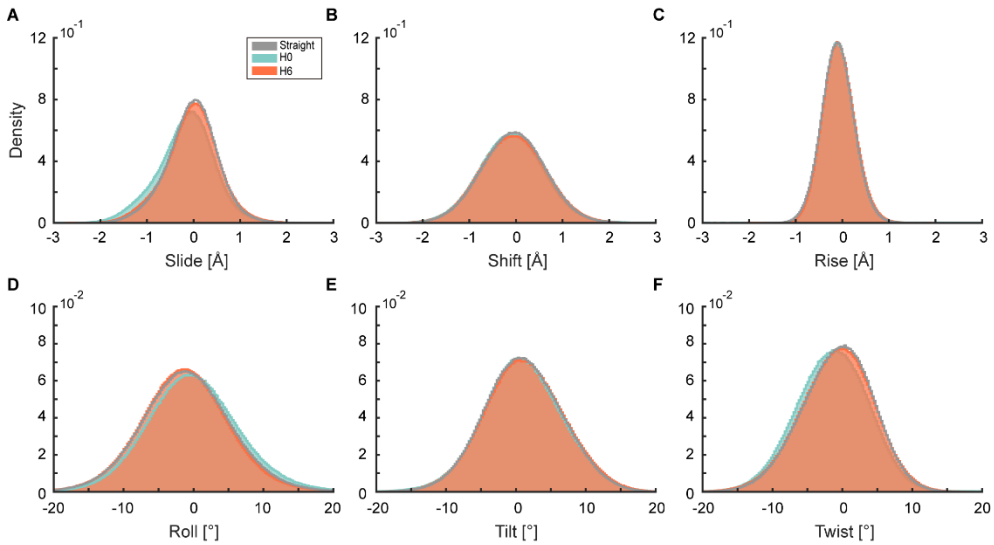

Figure 3-17. Distributions of deviations in BP step parameters. (**A**) Slide, (**B**) shift, (**C**) rise, (**D**) roll, (**E**) tilt and (**F**) twist. A deviation of BP parameters represents how different BP parameters in 6HB is from those of DNA duplex, which were taken from the MD simulation[31] summarized in Table 3-5.

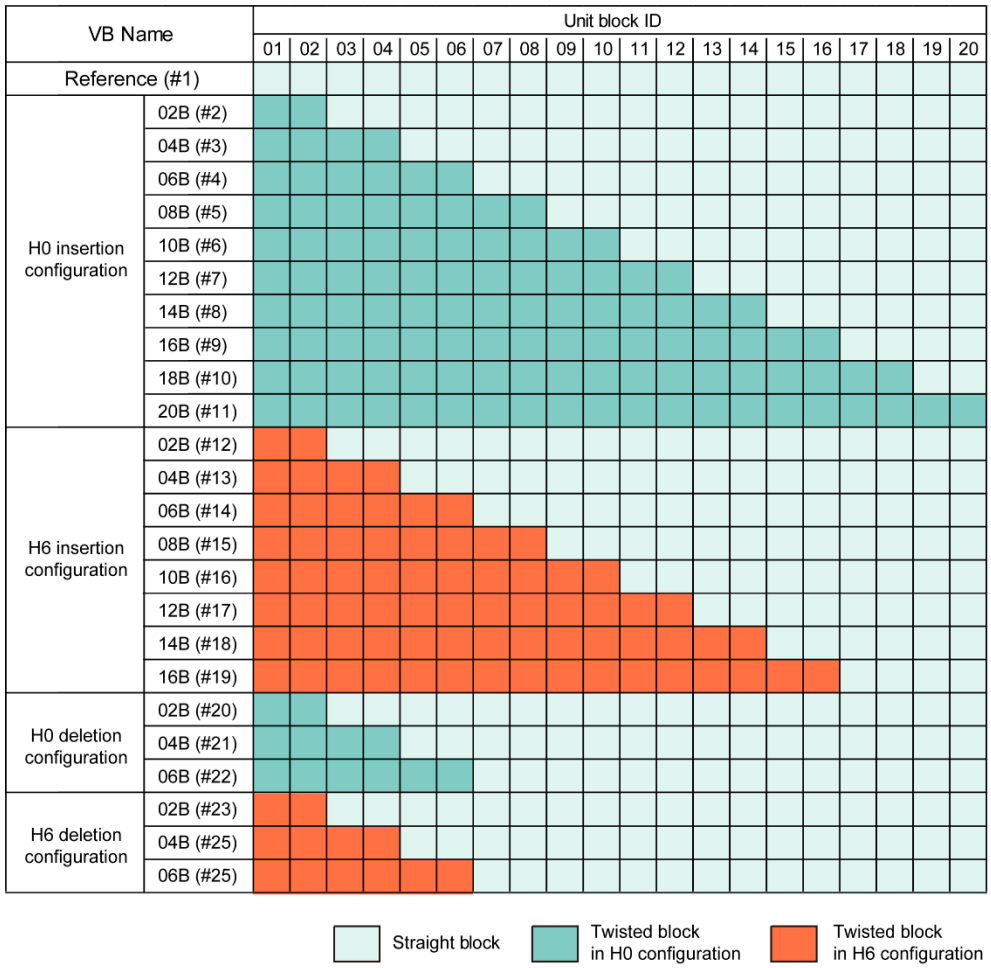

Table 3-1. **Unit block designs in VB**. Detailed designs of unit blocks in VB of 6HB structures used in Fig. 3-2C. We made different torsional variants of the reference structure by varying the number and the type of twisted blocks.

# of insertion blocks in H0 configuration	00	02	04	06	08	10
Monomer folding yield (%)	73.5	75.1	80.8	78.7	77.2	75.1

# of insertion blocks in H0 configuration	12	14	16	18	20
Monomer folding yield (%)	74.9	77.2	76.1	79.3	78.5

# of insertion blocks in H6 configuration	02	04	06	08	10
Monomer folding yield (%)	76.1	77.5	70.5	72.3	73.0

# of insertion blocks in H6 configuration	12	14	16
Monomer folding yield (%)	69.8	74.2	72.1

# of deletion blocks in H0 configuration	02	04	06
Monomer folding yield (%)	78.4	78.8	77.6

# of deletion blocks in H6 configuration	02	04	06
Monomer folding yield (%)	78.1	77.6	75.3

Table 3-2. **Monomer folding yield of all structures shown in Fig. 3-2C.** The monomer folding yield was calculated as the intensity ratio between the leading monomer band and all bands.

# of insertion blocks in H0 configuration	00	02	04	06	08	10
Number of samples (Images)	634 (6)	573 (6)	681 (6)	1228 (11)	617 (6)	438 (5)
TR	0.1325	0.1606	0.3333	0.5000	0.7017	0.7945
STD	0.0421	0.0393	0.0431	0.0602	0.0442	0.0337

# of insertion blocks in H0 configuration	12	14	16	18	20
Number of samples (Images)	502 (6)	659 (5)	900 (7)	871 (7)	418 (6)
TR	0.8088	0.5630	0.7100	0.4891	0.3871
STD	0.0180	0.0242	0.0390	0.0441	0.0516

# of insertion blocks in H6 configuration	02	04	06	18	20
Number of samples (Images)	535 (6)	661 (5)	516 (6)	540 (6)	535 (6)
TR	0.2785	0.5446	0.7907	0.8018	0.6542
STD	0.0313	0.0517	0.0157	0.0384	0.0571

# of insertion blocks in H6 configuration	12	14	16
Number of samples (Images)	416 (6)	518 (6)	528 (5)
TR	0.2885	0.1313	0.2975
STD	0.0179	0.0123	0.0248

# of deletion blocks in H0 configuration	02	04	06
Number of samples (Images)	403 (5)	1014 (9)	409 (4)
TR	0.1638	0.24458	0.3521
STD	0.0205	0.0502	0.0546

# of deletion blocks in H6 configuration	02	04	06
Number of samples (Images)	674 (6)	724 (6)	700 (6)
TR	0.2166	0.5082	0.7471
STD	0.0115	0.0650	0.0428

Table 3-3. **Detailed experimental data on TR shown in Fig. 3-2C**. STD represents of a standard deviation of TR values obtained from each image for each structure.

Crossover	Scale factor for stiffness		
	S	B	C
Rigid	1e5	1e5	1e5
Flexible	1	0.2	0.1

Table 3-4. **The crossover models used in CanDo analysis.** The rigid crossover model assumes crossovers as non-deformable ones. On the other hand, the flexible crossover model consider its flexibility in deformation. In the flexible crossover model, the axial stiffness (S) of crossover is assumed to be same with that of DNA duplex, the scale factor for torsion (C) was referred to the values obtained from MD simulations used in CanDo model for lattice-free structures[43] and the scale factor of 0.2 was chosen for bending stiffness (B) to reproduce the experimental results obtained from 6HB with 12 insertion blocks in H0 configuration.

Sequence step	Tilt [°]		Roll [°]		Twist [°]		Slide [nm]		Shift [nm]		Rise [nm]	
AA/TT	-3.62	4.34	6.17	5.52	36.4	3.99	-0.03	0.05	-0.01	0.04	0.34	0.03
AG/CT	-2.99	4.32	10.18	5.42	32.27	4.28	-0.03	0.06	-0.03	0.04	0.34	0.03
GA/TC	-1.11	5.16	3.7	5.64	39.02	4.25	-0.01	0.05	0.01	0.05	0.34	0.03
GG/CC	0.77	5.01	6.85	5.66	34.26	5.51	-0.01	0.07	-0.05	0.07	0.36	0.03
AC/GT	-0.5	4.78	5.03	5.86	32.1	5.09	0.04	0.06	-0.04	0.05	0.32	0.04
AT/AT	-0.13	4.13	3.33	5.79	31.97	4.14	0.02	0.07	-0.05	0.04	0.33	0.03
GC/GC	0.01	4.86	2.09	5.55	38.32	4.86	0.01	0.06	-0.04	0.04	0.34	0.03
TG/CA	1.04	5.22	13.57	7.00	32.27	5.11	0.00	0.07	-0.02	0.06	0.35	0.04
TA/TA	1.92	5.24	8.93	8.11	35.71	5.31	-0.02	0.07	0.01	0.07	0.35	0.04
CG/CG	-0.48	5.95	14.47	7.42	32.78	5.19	-0.03	0.06	0.02	0.05	0.35	0.04

Table 3-5. The sequence-dependent mean BP step parameters used in Fig. 3-17.[31]

3.4. Fine control over twist rate

By changing the number of BPs inserted into the helix segment of high strain energy per unit block, various twist rates can be programmed into the structure. Here, we designed five additional structures with six twisted unit blocks in VB whose insertion configurations were varied from H1 to H5 (Fig. 3-18 and 3-19 and Table 3-6). AFM image analysis showed that TR values of these structures monotonically increased with the number of high-strain-energy insertions from 0.57 to 0.74 bounded by those of H0 (0.50) and H6 (0.79) configurations, demonstrating fine controllability of the twist rate by the proposed configurational design of mechanical perturbation. The CanDo predictions with the flexible crossover model agreed quite well with the experimental results without any further revision for model parameters. The total twist angle of the structure achieved with H0 to H6 configurational designs was ranging from 86.5º to 150.7º, corresponding to the twist rate of 14.4º to 25.1º with a mean increment of 1.8º per unit block, which is comparable to the tunability over the bending angle of DNA origami structures[49, 65]. It was observed that this configurational variation for twist control did not affect the folding yield significantly (Fig. 3-18B and Table 3-7).

Further computational investigation on other insertion configurations using CanDo revealed that the most dominant factor for controlling the twist rate was the number of high-strain-energy insertions (Fig. 3-18 and 3-20). For example, while sixty-four (2^6) insertion configurations were possible in total when every helix had one inserted BP per unit block, only seven distinct twist rates were obtained corresponding to H0 to H6 configurational designs. When the number of high-strain-

energy insertion is the same, twist rates are almost same despite different insertion configurations. Similar results were also obtained even if the number of inserted BPs that each helix can possess per unit block was increased even though overall twist rates and their variation were slightly increased.

Our configurational design approach to finely modulate a twist rate can be easily applied to any other twisted structures with a different number of helices and a cross-sectional shape. To illustrate, we designed a fourteen-helix bundle (14HB) consisting of 24 unit blocks where a single BP was inserted into each helix per unit block. Axially varying insertion configurations were programmed where the number of high-strain-energy insertions was gradually increased by two every four unit blocks from H4 to H14 (Fig. 3-18D). Note that four inner helices have three adjacent helices unlike other ones, and therefore, there exist the 7-BP helix segments only when all possible crossovers form. CanDo analysis predicted that the twist angle of four unit blocks increased from 36.9º to 73.4º with the number of high-strain-energy insertions. Considering all possible insertion configurations from H4 to H14, the twist rate of 9.2º to 18.4º with a mean increment of 0.9º per unit block can be inscribed into this specific 14HB structure using the proposed method.

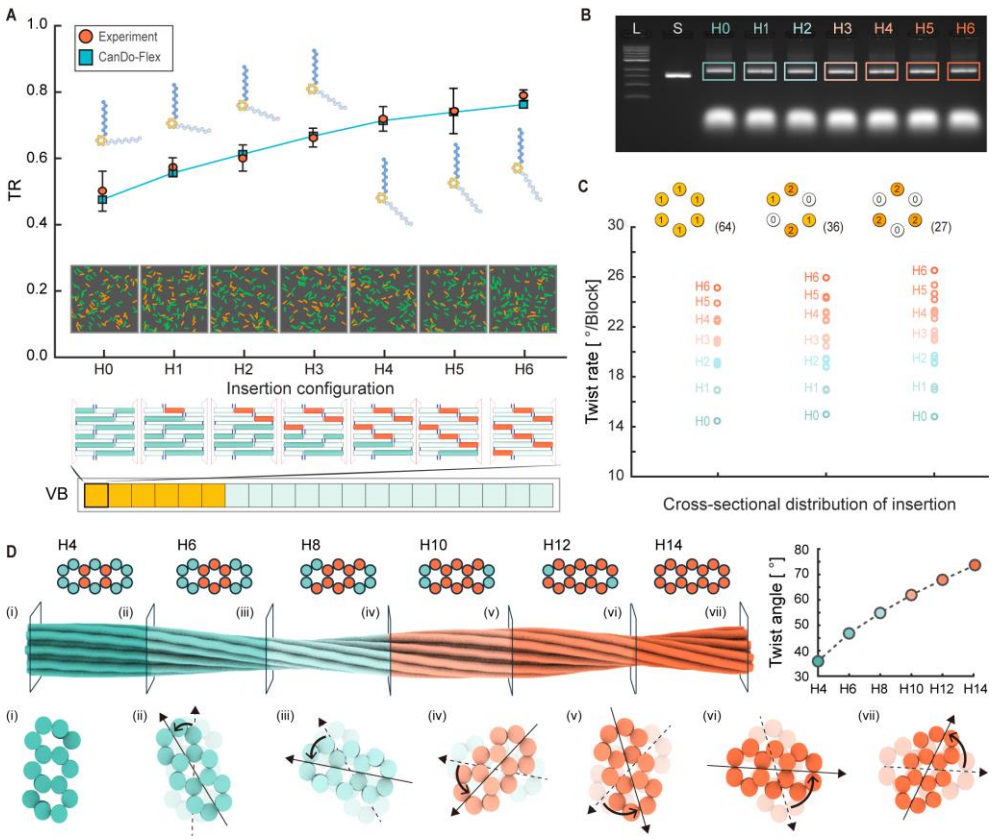

Figure 3-18. Fine control over twist rate. (**A**) TR variations with respect to the number of high-strain-energy insertions. Circles represent TR values by counting the number of cis- and trans-conformers in all AFM images. A solid line shows TR variations predicted by CanDo analysis with flexible crossover models. Cis- and trans-conformers are highlighted using orange and green colors, respectively, in the inset, modified AFM images. (**B**) Agarose gel electrophoresis results. Colored boxes are monomer structure bands and the bottom bands correspond to excessive staples. L and S denote 1kb DNA ladder and scaffold strand, respectively. (**C**) Twist rates for various cross-sectional distributions of insertions predicted by CanDo analysis with the flexible crossover model. Numbers in circles indicate the number of insertions in each helix per unit block. Numbers in the bracket at the bottom right corner of each

cross-section scheme indicate the number of all possible insertion configurations. (**D**) Demonstration of axially varying twist rate using a 14HB structure. Twist angles were calculated using CanDo analysis with the flexible crossover model.

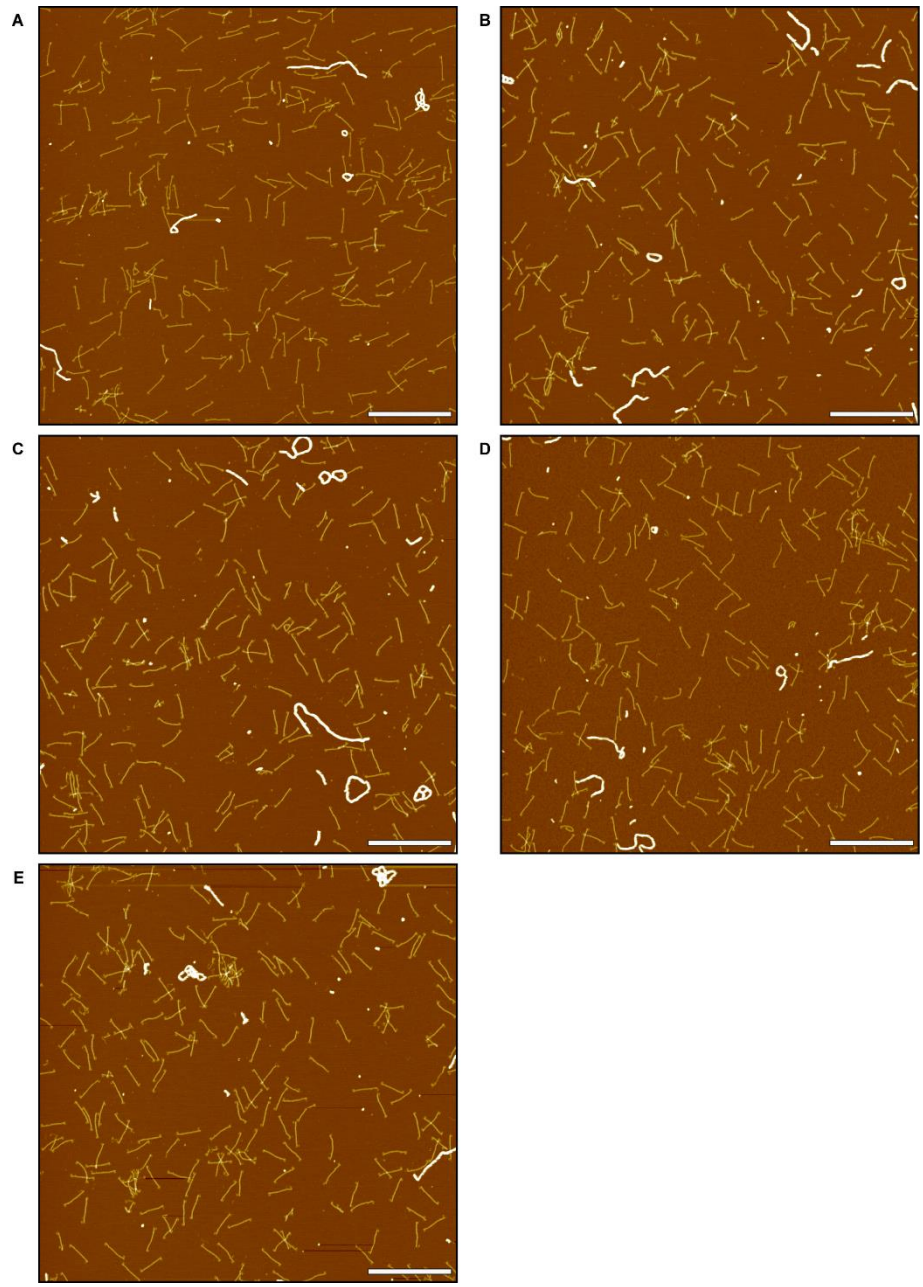

Figure 3-19. Representative AFM images of the structures shown in Fig. 3-18A.

Scale bars: 1 μm. 6HBs with 6 insertion blocks in (**A**) H1, (**B**) H2, (**C**) H3, (**D**) H4 and (**E**) H5 configurations.

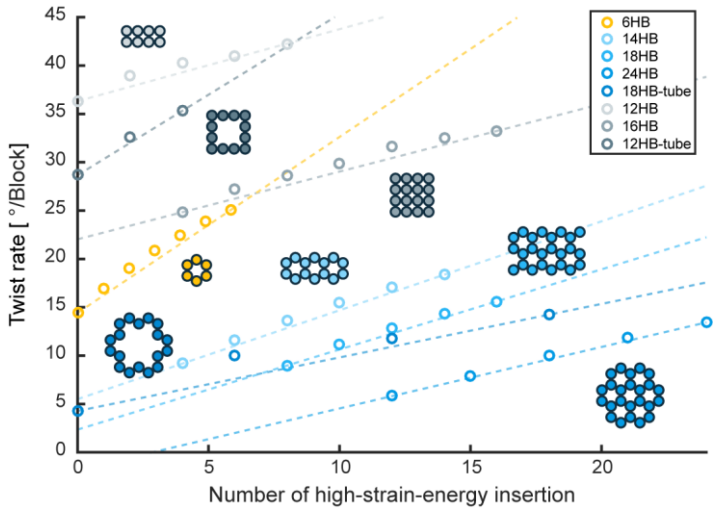

Figure 3-20. Twist rate of various cross-section in Fig. 3-1D. Applying the configurational design concept, we designed several variants of various cross-sections provided in Fig. 3-1D and measured their twist rates. From these computational experiments, we found that twist rate variations by the number of high-strain-energy perturbations can be well approximated by a simple, linear function for a given cross-section. Therefore, the number of high-strain-energy perturbations required for the target twist rate of any cross-section can be obtained from a linear function passing the two representative configurations, those with number maximum and the minimum number of high-strain-energy perturbations. Starting from this initial guess, it would be possible to obtain a target twist rate by iteratively varying cross-section distribution of them.

Insertion configuration	H0	H1	H2	H3	H4	H5	H6
Number of samples (Images)	1228 (11)	625 (6)	693 (7)	780 (7)	1420 (12)	599 (6)	516 (6)
TR	0.5000	0.5728	0.6002	0.6618	0.7183	0.7429	0.7907
STD	0.0602	0.0282	0.0396	0.0283	0.0372	0.0684	0.0157

Table 3-6. Detailed experimental TR data shown in Fig. 3-18A. STD represents of a standard deviation of TR values obtained from each image for each structure.

Insertion configuration	H0	H1	H2	H3	H4	H5	H6
Monomer folding yield (%)	78.9	79.9	83.1	82.6	83.1	81.7	79.8

Table 3-7. Monomer folding yield of all structures shown in Fig. 3-18B. The monomer folding yield was calculated as the intensity ratio between the leading monomer band and all bands. Using six twisted blocks in VB, the insertion pattern of the twisted block was varied from H0 to H6 pattern.

3.5. Twist control assisted by mechanical relaxation using gaps

While inserted or deleted BPs introduce the mechanical strains into the structure, gaps (short unpaired NTs) are, on the other hand, known to relieve them therein. This structural characteristic has been utilized, for example, to alleviate the accumulated strain energy in the structure designed on a square lattice[57]. While we showed the effectiveness of the configurational design of inserted or deleted BPs so far, a similar design approach can be employed to program mechanical relaxation into the structure as well.

To demonstrate, we utilized gaps as strain-releasing structural motifs to locally lower the strain energy induced by inserted BPs. In practice, gaps can be easily introduced into the structure by replacing staple strands at nick positions with shorter ones (Fig. 3-21A). The level of relaxation was tuned by the gap length (the number of unpaired NTs in a gap) and the gap density (the number of nicks replaced by gaps divided by the total number of nicks per unit block).

Six variant structures were designed and constructed by incorporating different gap motifs into the original twisted structure consisting of six insertion blocks with H0 configuration. Two gap lengths (1- and 3-NT) and three gap densities (1/3, 2/3, and 1) were considered. Clear monomer bands were observed in agarose gels (Fig. 3-22 and Table 3-8) and no significant shape distortion was found in AFM images (Fig. 3-23 and Table 3-9) for all structures. Higher reductions in TR value (or twist angle) were observed for higher gap densities and longer gap lengths (Fig. 3-21B). The twist angle could be decreased by up to 30º when 3-NT-long gaps were used with full gap density as indicated by TR values reduced from 0.5 to 0.17. These

results suggest that incorporating the mechanical relaxation *via* gaps into the configurational design approach would further widen the controllable range of twist angle with fine tunability.

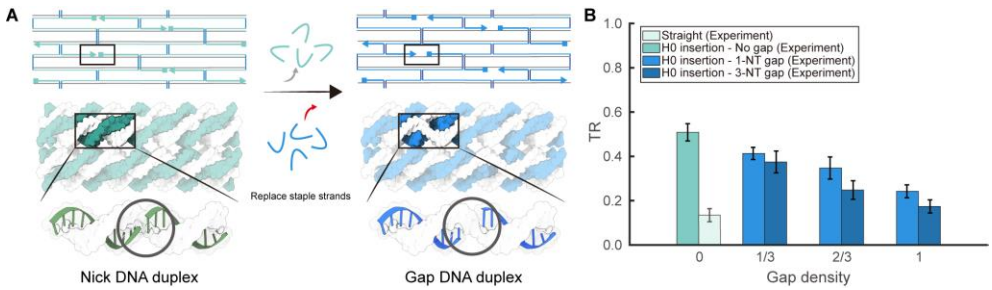

Figure 3-21. Twist control by mechanical relaxation using gaps. (**A**) Design scheme of an insertion block with gaps. Nicks are locally changed into gaps with different lengths by replacing staple strands at nick positions with shorter ones. (**B**) TR variations with respect to the gap density and length. All results used in Figure 4B are obtained from experiments.

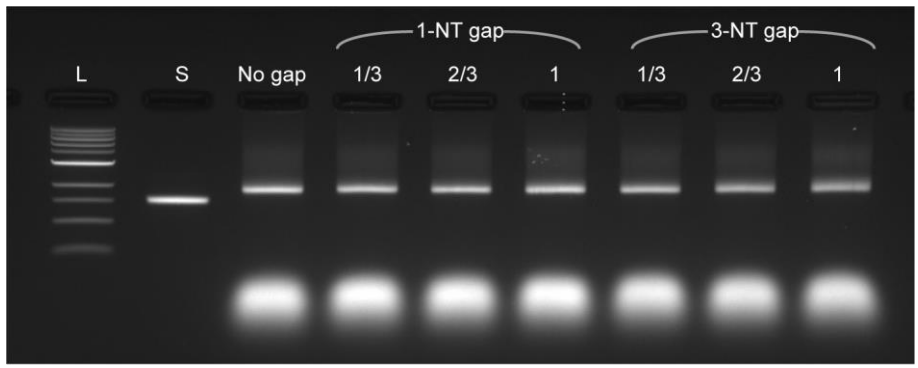

Figure 3-22. Agarose gel electrophoresis results of the structures shown in Fig. 3-21B. For the 6hb using six H0 insertion blocks in VB, density and length of gaps are varied. L: 1kb DNA ladder and S: Scaffold strand.

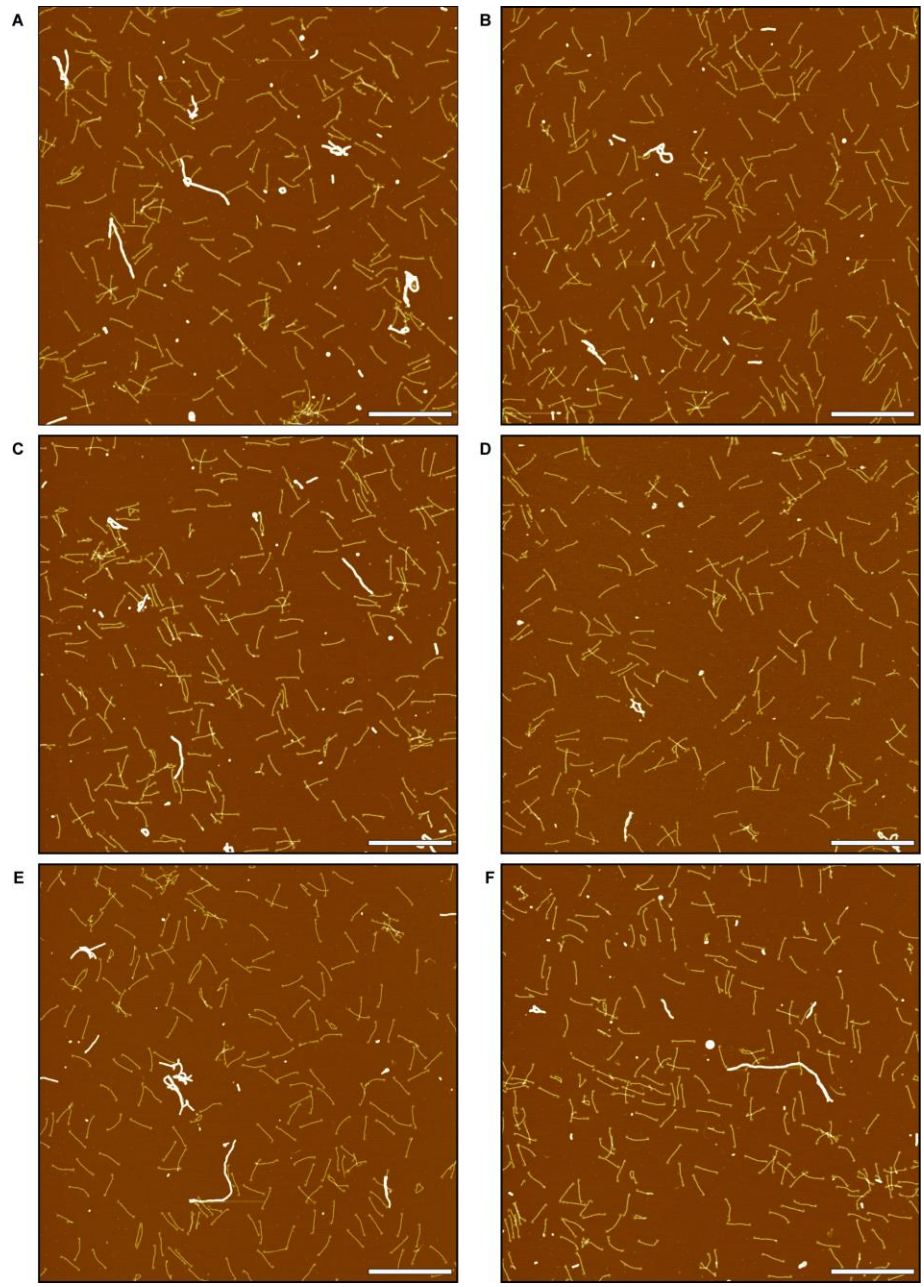

Figure 3-23. Representative AFM images of the structures shown in Fig. 3-21B.

Scale bars: 1 μm. 1-NT gap with gap densities of (**A**) 1/3, (**B**) 2/3 and (**C**) 1. 3-NT gap with gap densities of (**D**) 1/3, (**E**) 2/3 and (**F**) 1.

Insertion configuration	No gap	1-NT gap 1/3	1-NT gap 2/3	1-NT gap 1	3-NT gap 1/3	3-NT gap 2/3	3-NT gap 1
Monomer folding yield (%)	74.2	84.7	84.6	81.6	83.7	83.2	76.6

Table 3-8. Monomer folding yield of all structures shown in Fig. 3-22. The monomer folding yield was calculated as the intensity ratio between the leading monomer band and all bands.

Insertion configuration	No gap	1-NT gap 1/3	1-NT gap 2/3	1-NT gap 1	3-NT gap 1/3	3-NT gap 2/3	3-NT gap 1	Straight
Number of samples (Images)	1228 (11)	963 (8)	655 (6)	590 (5)	982 (9)	605 (5)	609 (5)	634 (5)
TR	0.5000	0.4133	0.3476	0.2424	0.3747	0.2479	0.1740	0.1325
STD	0.0602	0.0499	0.0396	0.0294	0.0495	0.0421	0.0294	0.0421

Table 3-9. Detailed experimental TR data of the structures shown in Fig. 3-21. STD represents of a standard deviation of TR values obtained from each image for each structure.

3.6. Summary

In summary, programming the spatial distribution of strain energy offers a versatile way of modulating the twist rate of DNA origami structures at a high resolution, thereby widening the feasible design space for twisted structures. Our configurational design method is cost-effective as it requires strand replacements locally only at the twisted unit blocks whose twist rate needs to be adjusted. While we utilized BP insertions/deletions and gaps for controlling the strain energy distribution in this study, other methods can be used alternatively including selective crossover removals which would locally vary the crossover spacing. The proposed approach can be easily extended to the design of more complex structures such as helical coils[50] with spatially varying curvature and twist rate. Therefore, it is expected to be useful in constructing functional twisted structures to optimize, for example, the optical response of plasmonic structures[11], the release kinetics of drugs from therapeutic structures[55], or precisely modulating the orientation of molecules of interest together with their location.

Chapter 4. Mechanical stress engineering for shape reconfiguration

4.1. Limitation in the reconfiguration mechanisms

Through reactions generating geometric changes of dsDNA, the mechanical stress can be introduced after the self-assembly. For example, a canonical geometry of dsDNA can be easily perturbed through Ethidium Bromide (EtBr) binding. It showed its great potential as a versatile mechanical stress source enabling a reversible and even progressive reconfiguration of DNA origami structures. Since EtBr binding causes only uniform twist along an axial axis of the DNA origami structure, however, it is difficult to achieve bending deformation resulting in limitations in structural diversity of reconfigured shapes and its utility as functional nanomachines. Although UV light with short wave length can make similar structural changes in dsDNA[51], the change is irreversible and spatial control of it is also difficult to achieve.

To this end, here, we suggest a reconfiguration mechanism, called the homeomorphic transformation, using a topological constraint of the closed structure. When topologically constrained, a linking number should be conserved. This topological invariant property enables transformation of the torsional deformation into the bending one. To illustrate, we designed the six-helix-bundle (6HB) ring and reconfigured it into the supercoils with different crossing numbers (N_{SC}) depending on the EtBr concentration introduced. Also, we found a torsional buckling occurred during the transition between a ring and a figure-eight shape conformations, the

supercoil with N_{SC} of one. Properties of the homeomorphic transformation including a critical EtBr concentration for buckling transition and increase rate of crossing number can be adjusted by flexibility of the 6HB ring controlled through gaps, short unpaired nucleotides (NTs).

`

4.2. Buckling-induced homeomorphic transformation

Joining both ends of a linear structure makes it closed so that the free rotation of its ends becomes impossible. Under this topological constraint, the linking number (L_k), the sum of the writhe (W_r) and the twist (T_w), of the structure should be conserved despite any deformation applied. The invariance of L_k makes W_r and T_w coupled each other. Therefore, any change in either one of them is necessarily accompanied by change in the other. It provides a chance to reconfigure a simple two-dimensional structure into a complex three-dimensional one. Employing the topological property, here, we show a morphing mechanism of DNA origami structures, called the homeomorphic transformation .

Using DNA origami method[49, 66], to illustrate, we designed a closed 6HB ring with no twist along its axial axis (Figs. 3-1 to 3-3). Since there is no W_r and T_w in the 6HB ring, it has a zero L_k in its relaxed state. To alter the T_w of the 6HB ring, we introduced EtBr, a representative intercalating molecule. EtBr is well known to perturb a canonical geometry of B-form dsDNA, especially lowering a twist angle by 26º between neighboring base-pairs (BPs)[52]. Since helix segments within DNA origami structures are constrained by crossovers connecting adjacent helices, the geometrical perturbation of dsDNA induced by EtBr binding causes mechanical torsional stress leading to the negative (*i.e.*, left-handed) twist of DNA origami structures along their axial axis[53-54]. While a linear structure with no topological constraint is simply twisted along its axial axis due to EtBr binding and its L_k would be decreased, a closed structure like the 6HB ring would be not only twisted but also bent, or writhed, to conserve the linking number after EtBr binding. The writhe induced by EtBr-driven twist enables the circular 6HB ring to be reconfigured into

various the 6HB supercoils with the same $L_{k,}$ which are homeomorphic monomers of the 6HB ring.

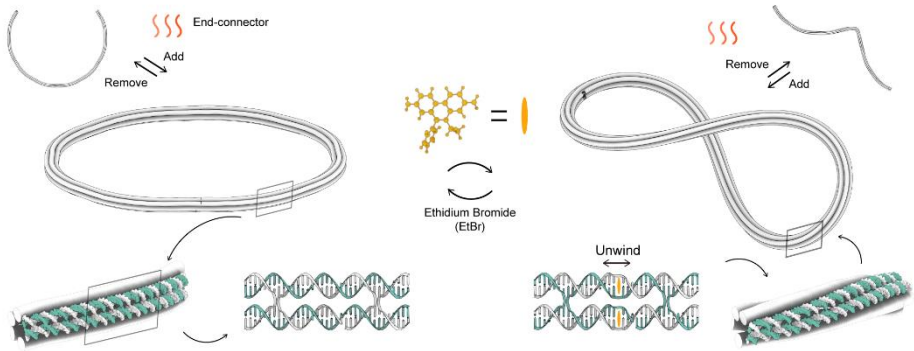

Figure 4-1. Illustration of the homeomorphic transformation of DNA origami structures. The 6HB ring can be reconfigured into the 6HB plectonemic supercoil through torsional stress induced by intercalation of EtBr.

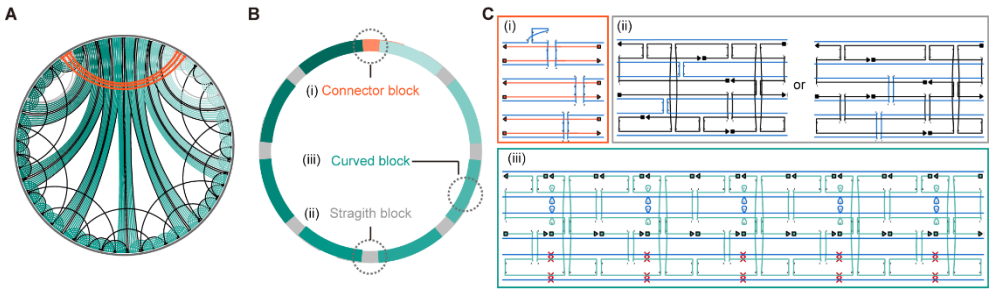

Figure 4-2. Detailed design schemes for the six-helix-bundle (6HB) ring. (A) A circular graph showing connectivity of staple strands. The outer, circular gray-colored line represents a scaffold strand. The green-colored lines represent staples used in the curved blocks shown in (B). The black-colored lines represent staples in the straight blocks. The red-colored lines represent staple strands connecting both ends of the ring. (B) A block scheme of the 6HB ring showing. Since scaffold crossovers exists in the straight and the connector blocks, we do not introduce the inserted or the deleted base-pairs (BPs). (C) The caDNAno diagrams representing a scaffold routing and connectivity of staple strands for (i) the connector block, (ii) the straight block and (iii) the curved block.

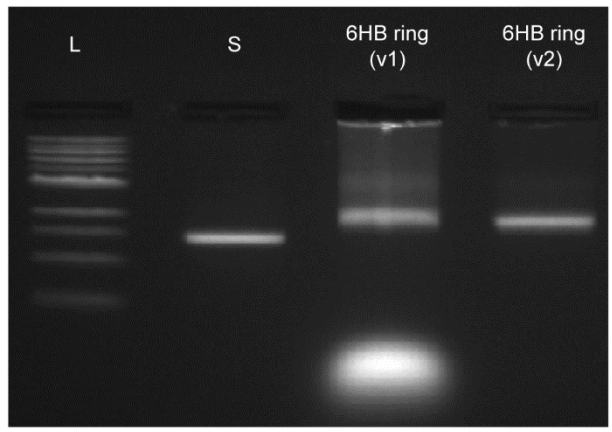

Figure 4-3. Agarose gel electrophoresis results of the 6HB ring. A clear monomer band was observed in the annealed sample (6HB ring-v1). To avoid unwanted EtBr binding to excessive staple strands, we performed buffer exchanges five times and confirmed that there was no remained staple strands (6HB ring-v2). L: 1kb DNA ladder and S: Scaffold strand.

4.3. Supercoiling of the 6HB ring

We explored experimentally the shape controllability of the proposed homeomorphic transformation method. To control reconfigured shapes of the 6HB ring whose radius is 61.64 nm (Fig. 4-4), we varied concentration of EtBr from 0 to 20 μM for the 6HB ring of 0.5 nM (Figs. 4-5A, 4-6 to 4-8). We quantified conformational shapes of 6HB homeomorphic monomers by measuring the average self-crossing number (N_{SC}) of the 6HB monomers from the atomic force scope (AFM) images (Fig. 4-5B). For each EtBr concentration, we analyzed at least 400 monomers to calculate N_{SC}. The N_{SC} of each monomer was calculated by counting the number of points with relatively brighter pixel values representing a higher height due to self-crossing (Fig. 4-5C). Depending on the concentration of EtBr, we observed various 6HB homeomorphic monomers with different N_{SC}, from 0 to 4. As N_{SC} increases, a size of loops at both ends of them got smaller increasing their curvature. Using transmission electron microscope (TEM), also, we confirmed not only similar conformational shapes but also more detailed shapes, the separation between distant regions of the 6HB monomer, between neighboring self-crossing points when N_{SC} is larger than 1 (Fig. 4-5C). In fact, it was difficult to resolve the shapes between neighboring self-crossing points in AFM images probably due to a relatively low resolution of AFM.

We identified three distinct phases classified by the variation of N_{SC} upon increase of EtBr concentration (Fig. 4-5A). In the first phase, contrary to our expectation, there was no noticeable change in N_{SC} despite of addition of EtBr by 1 μM and then an abrupt increase of N_{SC}, the onset of the supercoiling of the 6HB ring, was observed at 1.1 μM of EtBr. In the second phase, N_{SC} increased almost linearly

until EtBr concentration increased to 6 μM. The higher the EtBr concentration, the larger NSC was obtained. The results of the second phase were well approximated by a linear fit with a N_{SC} increase of 0.47 per 1 μM of EtBr. This linear behavior would make it possible to predict reconfigures shapes for a given EtBr concentration or determine the required EtBr concentration for a target reconfigured shape. In the third phase, N_{SC} was no longer increased by more than 3.20 at higher concentration of EtBr due to saturation effect. The saturation was probably due to a decrease in the binding affinity between EtBr and the 6HB monomers, which was previously observed.[54, 67] As the EtBr concentration increased, a ratio of the 6HB monomers with kink increased (Fig. 4-9A). It might be because the higher the concentration of EtBr, the larger curvature in the loop, resulting in larger strain energy, which makes it easier for the local kink to occur. However, similar results were observed regardless of whether the kinked monomers were included in calculation of N_{SC}.

We confirmed that the homeomorphic reconfiguration is reversible. To this end, we measured N_{SC} after adding 2 μM of EtBr and removing it by buffer exchange[19] (Figs. 4-10 and 4-11). Results showed that only one buffer change was enough to turn the 6HB supercoils back to the 6HB circle. Also, N_{SC} after adding 2 μM of EtBr again was almost same with the one measured when EtBr was added to the pure 6HB ring implying that there was little EtBr left after only one buffer exchange.

To confirm importance of the topological constraint, furthermore, we characterized an open 6HB ring by removing strands connecting both ends of the open 6HB ring under different EtBr concentration (Figs. 4-12 and 4-13). The open 6HB ring was deformed even at low concentration (= 0.5 μM) of EtBr. As EtBr

bound, the open 6HB ring was just twisted along its axial axis leading to helical coils. In other words, Lk of the open 6HB ring would increase upon addition of EtBr since there is no constraint at both ends. As more EtBr was added, a radius and a pitch of the 6HB helical coil became smaller and larger, respectively. This difference in reconfigured shapes mode showed the importance of topological constraint in supercoiling and buckling transition.

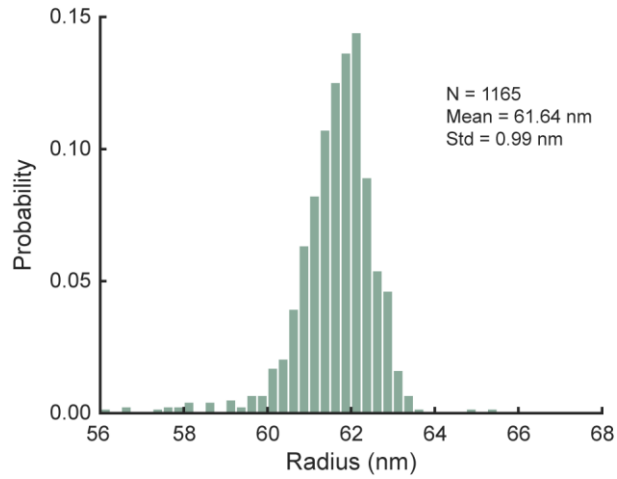

Figure 4-4. A histogram for radius of the 6HB ring.

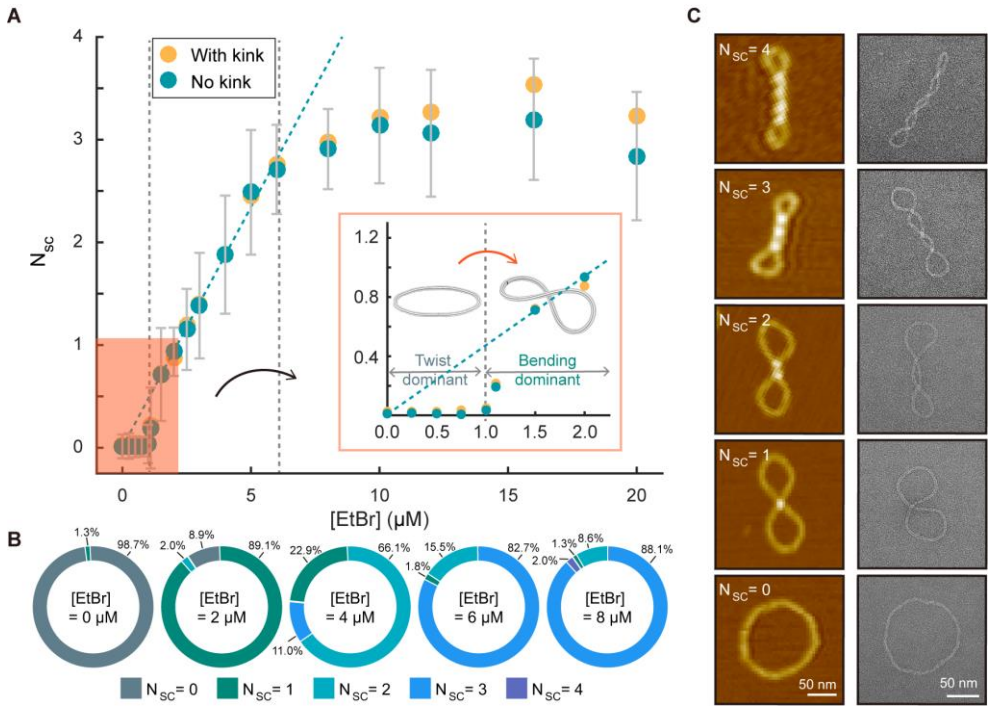

Figure 4-5. Homeomorphic transformation of the 6HB. (A) N_{SC} values measured experimentally for different EtBr concentrations. Regardless of whether kinked monomers are included in measuring N_{SC}, similar results were obtained. A plot of N_{SC} for low concentration of EtBr is enlarged in the inset to clarify an abrupt increase of N_{SC} representing torsional buckling. (B) For representative EtBr concentrations, summary of distribution on the 6HB homeomorphic monomers. (C) AFM (left) and TEM (right) images for the 6HB homeomorphic monomers with different N_{SC}. An illustration of the homeomorphic transformation of DNA origami structures.

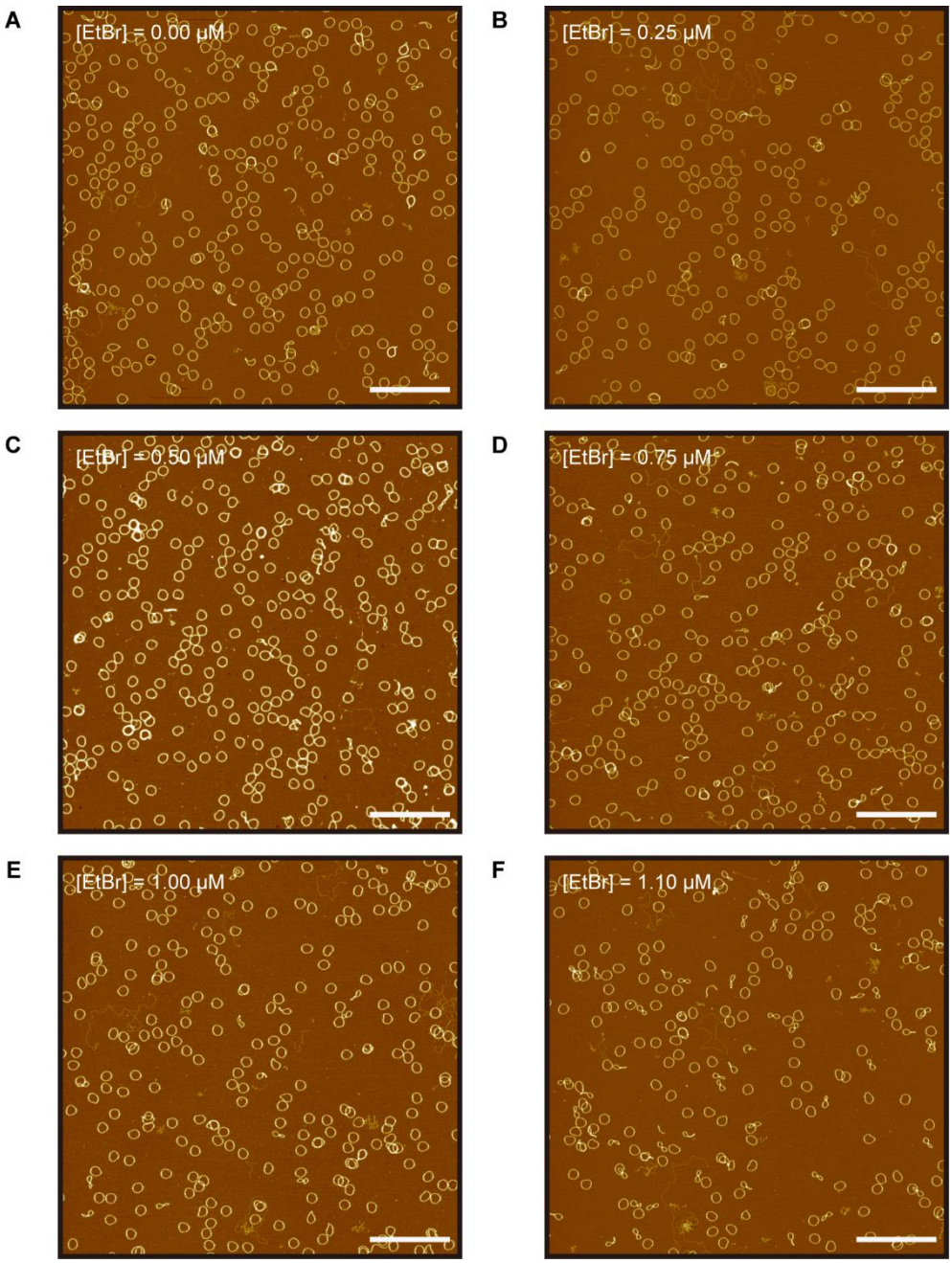

Figure 4-6. Representative AFM images of the 6HB ring for different EtBr concentrations. AFM images for samples in provided in Fig. 4-5A. Scale bars: 1 μm.

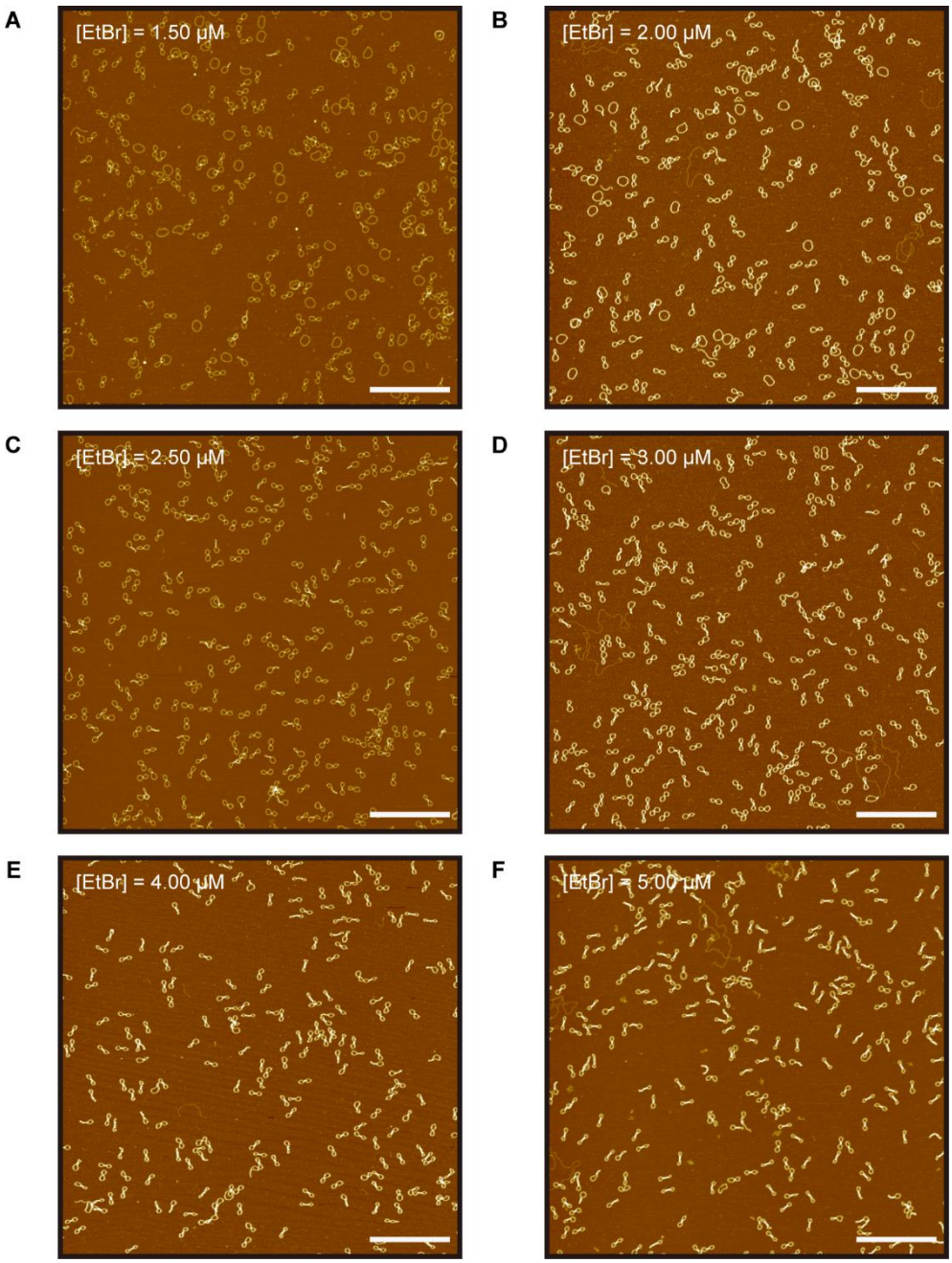

Figure 4-7. Representative AFM images of the 6HB ring for different EtBr concentrations. AFM images for samples in provided in Fig. 4-5A. Scale bars: 1 μm.

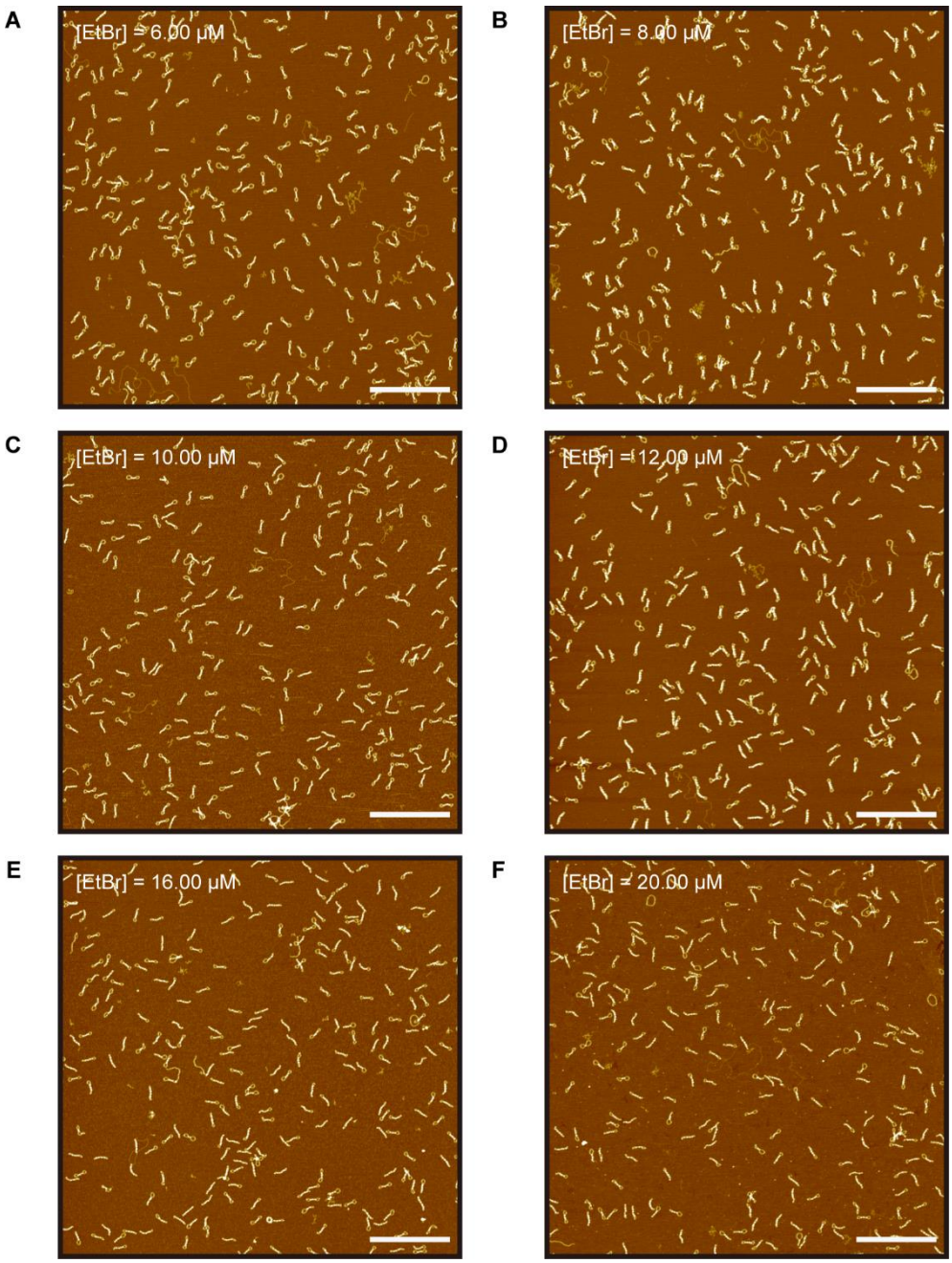

Figure 4-8. Representative AFM images of the 6HB ring for different EtBr concentrations. AFM images for samples in provided in Fig. 4-5A. Scale bars: 1 μm.

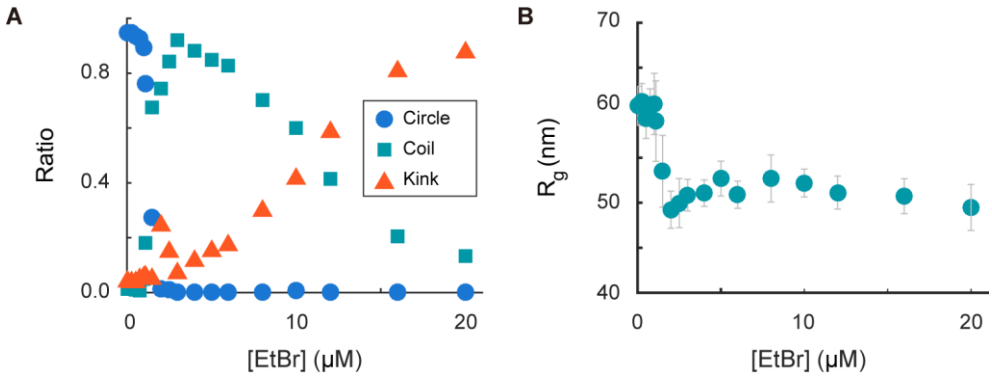

Figure 4-9. Image analysis of the 6HB monomer. (A) As the EtBr concentration increases, a ratio of the circular conformation decreases and also a ratio of kinked monomers increases, too, probably due to increased bending stress. (B) Using only non-kinked 6HB monomers, gyration radius (R_g) values measured experimentally for different EtBr concentrations.

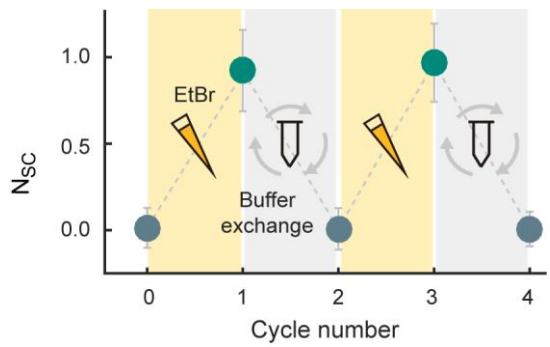

Figure 4-10. Reversibility of the homeomorphic transformation.

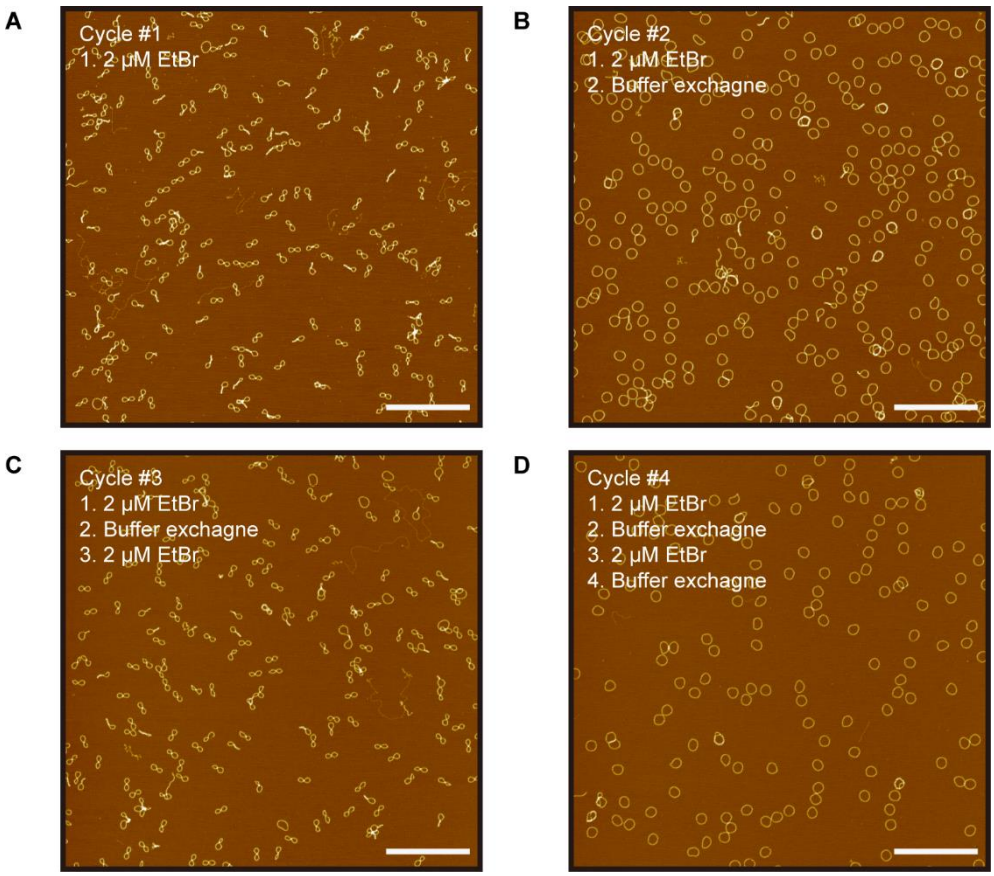

Figure 4-11. Representative AFM images of the 6HB ring for reversibility test.

AFM images for samples in provided in Fig. 4-10. Scale bars: 1 μm.

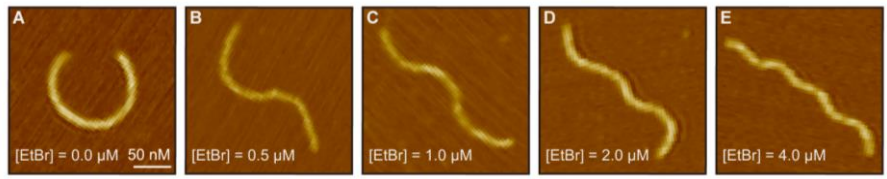

Figure 4-12. Conformations of the open 6HB ring. AFM images for the open 6HB circle for different EtBr concentrations.

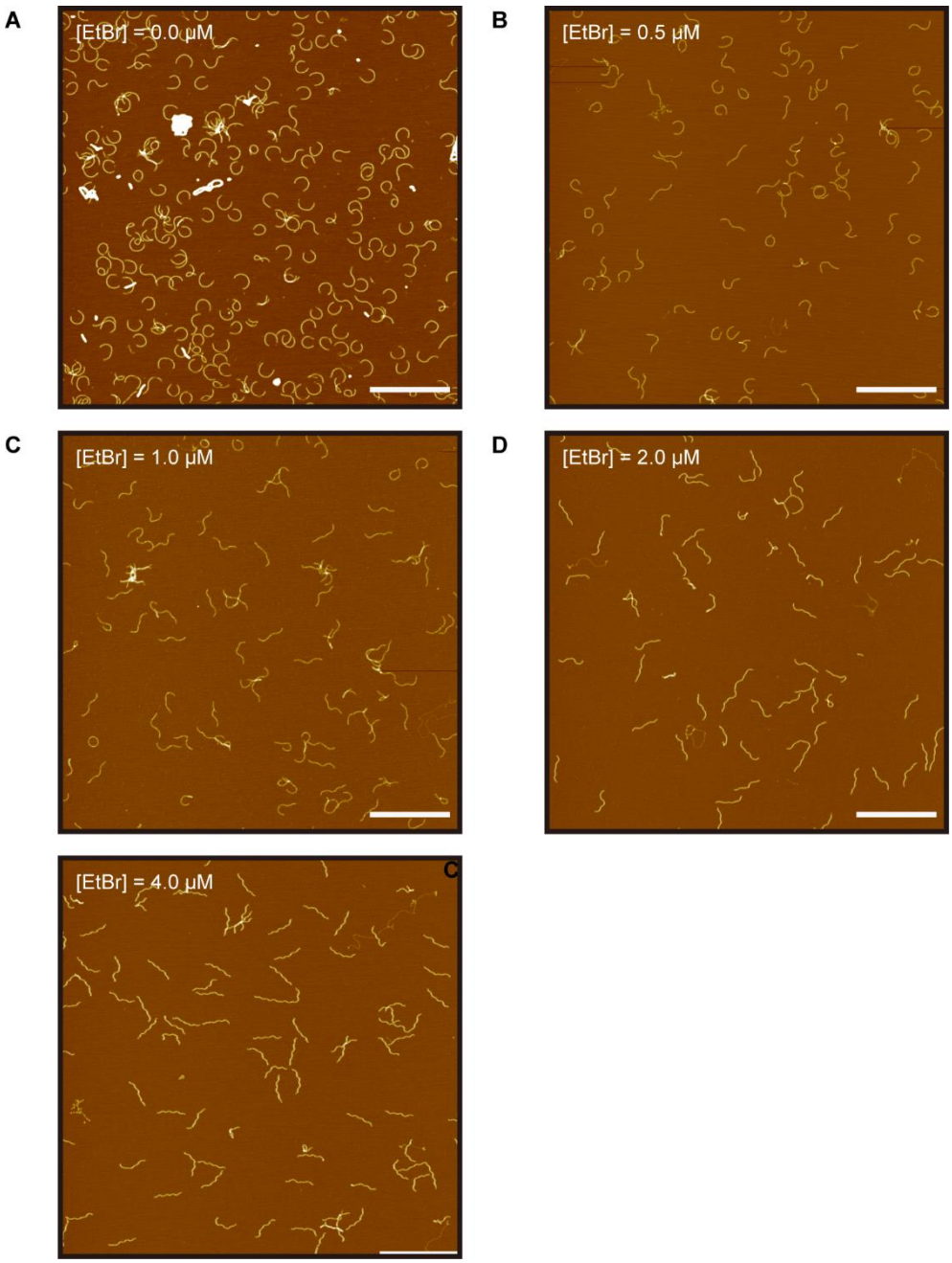

Figure 4-13. Representative AFM images of the open 6HB ring for different EtBr concentration. AFM images for samples in provided in Fig. 4-12. Scale bars: 1 μm.

4.4. Computational analysis of the buckling-induced supercoiling

To understand an origin of the sudden increase in N_{SC} of the 6HB monomer in the first phase (Fig. 4-5A), we simplified the problem into a dsDNA ring consisting of 336 BPs and analyzed its configurational changes (from a circle to coils) upon decrease of twist angles between neighboring BPs using finite element (FE) method (Appendix A3).

We found that the FE model predicted similar conformational changes to the ones observed in experiment. When the magnitude of decrease in θ was smaller than a certain critical value, $\Delta\theta_C$ (= 0.92º/BP in the dsDNA ring), the ring structure maintained its circular shape with no change in both W_r and T_w and only its torsional strain energy increased (Figs. 4-14A and B). This implied that EtBr binding might cause torsional strain energy of the 6HB ring without change in T_w before EtBr concentration exceeded 1 μM. When the magnitude of decrease in θ exceeded the $\Delta\theta_C$, however, we observed that out-of-plane displacements occurred suddenly due to buckling. And then a ring was progressively reconfigured into a coil with $N_{SC} = 1$, the figure-eight shape. While the torsional strain energy decreased (T_w increased), also, the bending strain energy increased (W_r decreased) (Fig. 4-14B). This results showed that the change in twist induced by EtBr binding might be converted to W_r resulting in conformational changes. Although results would be quantitatively different due to differences in geometrical and mechanical properties, our model can show qualitatively similar features found in conformational changes of the 6HB ring providing insights for understanding the buckling transition of the 6HB ring.

A buckling transition of a circle occurred is known as Michell's instability (Fig. 4-15).[68] For the dsDNA ring, we found that a critical value of twist (N_{Tw}) for buckling instability predicted by the Michell's equation (0.87 turn) is consistent with our FE simulation. Similarly, a value of N_{Tw} of the 6HB ring (6.14 turn) was calculated by the Michell's equation using mechanical properties of the 6HB.[28] For comparison, we performed CanDo analysis[41-42] to estimate the critical twist (N_{Tw}) for the experimentally observed buckling instabilty. We, first, converted binding density of EtBr into effective twist angle changes of dsDNA in the 6HB ring assuming EtBr binding unwinds dsDNA by 26º. Then, we calculated three-dimensional equilibrium shapes of only the curved block (Fig. 4-2B) using CanDo framework[41-42] and measured a twist rate of the 21-BP-long unit block in it for given binding density. A twist rate was calculated according to the literature (Appendix A1). Assuming the 6HB ring consists of 57 curved blocks, we estimated total twist angles for given binding densities. Therefore, we obtained a plot for the total twist angle versus binding density (Fig. 4-16). Our results showed that the total twist angle is linearly proportional to EtBr binding density. According to the previous report[53], the binding density of EtBr was 0.039 molecule/BP at 1 μM. Then, the estimated total twist would be 1.46 turn with left-handedness. However, the N_{Tw} value predicted by the Michell's equation (6.14 turn) was significantly larger than the estimated one (1.46 turn) using CanDo analysis. This implied that significant changes might occur in both bending and torsional rigidity due to EtBr binding[69].

The abrupt change in conformational shapes of the 6HB monomer due to buckling instability was observed similarly in a gyration radius (R_g) change (Fig. 4-

9B) because supercoiling made the 6HB monomers compact. However, it was difficult to tell any difference between the 6HB supercoils with different N_{SC}.

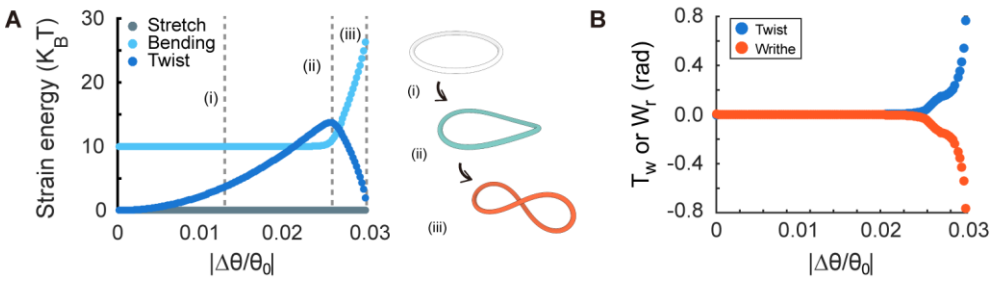

Figure 4-14. FE analysis on the dsDNA ring. (A) Decreasing a twist angle between neighboring BPs, the strain energy change was calculated. Representative conformational shape were visualized, together. (B) Measurement of the twist and the wirhte of the dsDNA ring. The twist for the dsDNA ring was calculated and the writhe was obtained considering that there is no linking number change. Θ_0 is 34.29º.

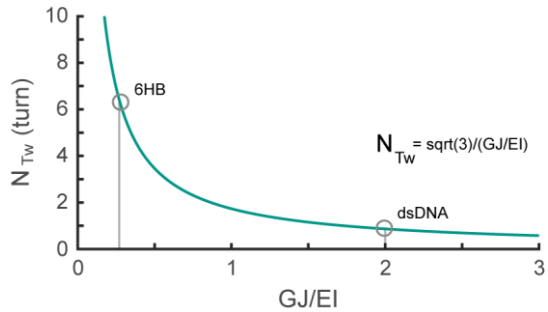

Figure 4-15. Prediction on the critical twist (N_{Tw}) for buckling transition. A plot was obtained from an analytical equation for the (N_{Tw}) that Michell provided[68]. The N_{Tw} is determined by GJ and EI, which are torsional and bending rigidity of the ring, respectively. According to the Michell's equation, a torsional buckling would occur at N_{Tw} of 0.87 and 6.14 turn for dsDNA and 6HB, respectively.

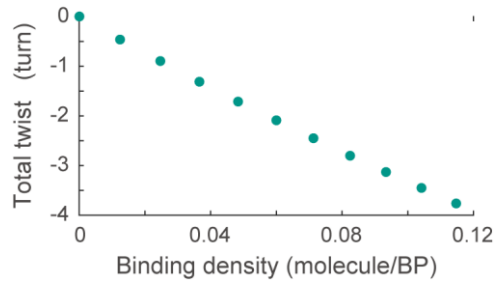

Figure 4-16. Estimation on the twist induced by EtBr binding. Assuming EtBr binding unwinds dsDNA by 26º, we calculated effective helicity change of the 6HB ring and the total twist angle caused by change in the effective helicity using CanDo framework.

4.5. Reconfiguration control by local defects

Mechanical stress, a driving force for the homeomorphic transformation, in DNA origami structures can be controlled by not only the EtBr binding, but also introduction of short unpaired NTs, gaps, therein. For example, recently, we showed that that mechanical stress caused by inserted BPs can be regulated through engineering local flexibility of the straight 6HB with gaps leading to a broader controllability on twist angle of the structure.[27] A similar mechanical design approach can be employed to engineer reconfigured shapes of the 6HB homeomorphic monomers. To demonstrate, we introduced gaps in the 6HB ring as a structural motif to mitigate mechanical stress induced by EtBr binding (Fig. 4-17A). The gap can be introduced by simply replacing staple strands at nick positions with shorter ones. With the 3-NT-long gaps, we adjusted the level of stress relaxation by varying gap density (the number of nicks replaced by gaps divided by the total number of nicks). Two gap densities (half and full) were considered. The 6HB ring consists of the eight curved blocks along its axial axis (Fig. 4-2B). In case of the half gap density, gaps were inserted in only four of the total eight blocks at two blocks interval. N_{SC} was measured for the 6HB ring with different gap densities given various EtBr concentration. Higher reduction in N_{SC} was observed for the higher gap density (Figs. 4-17B). This higher reduction suggested that the mechanical stress relaxation through gaps would enable engineering homeomorphic transformation behaviors without change in EtBr concentration. For a given concentration, less mechanical stress was induced when gap motifs were introduced. Also, this leads to increase of the critical concentration for the buckling transition.

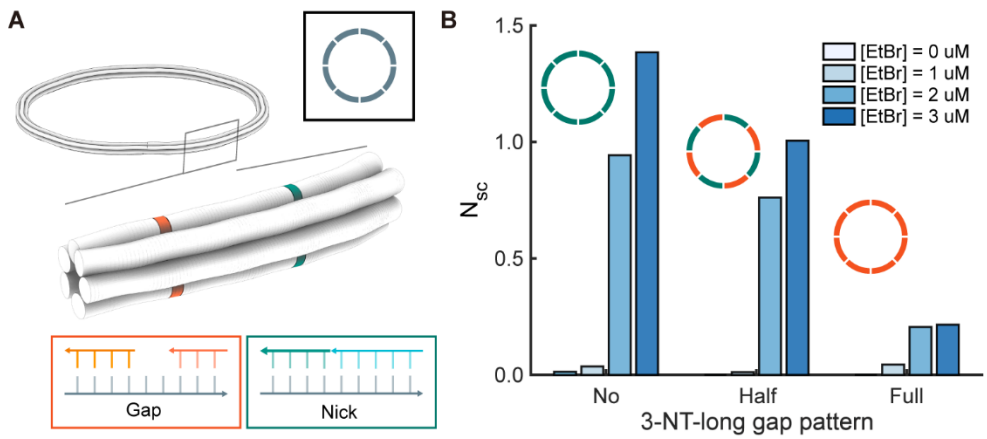

Figure 4-17. Configuration control by local defect. (A) An illustration of gap and nick motifs in the 6HB ring. (B) N_{SC} values for the 6HB ring with different gap designs.

4.6. Summary

In summary, our reconfiguration mechanism using the topological invariant property offers a simple, on-demand way of changing conformational shapes of the DNA origami structure by transforming local twist deformation into global bending deformations. Through relaxation of the induced mechanical stress, also, engineering local flexibility allows us to control characteristics of buckling transition between the circular and the supercoiled shapes. Integrated with stimuli-responsive motifs that dynamically change local flexibility, our system could be applied to development of mechanically reconfigurable devices responding to external cues. For example, a photo-responsive reversible reconfiguration could be achieved in combination with azobenzene-modified nucleotides[70], which would be our future work. We expect that these dynamic systems would be utilized for dynamic rearrangement of functional materials enabling control of their cooperative behaviors like plasmonic coupling and enzyme cascade.

Chapter 5. Concluding remark

In this thesis, we presented two design strategies for engineering mechanical stress to achieve the fine shape control of the DNA origami structure and the reconfiguration into a complex three-dimensional target configuration, respectively. First, the fine control over the twist rate was demonstrated by the configurational design of mechanical perturbations, which spatially programs distributions of inserted or deleted BPs and therefore controls the induced strain energy. Second, the reconfiguration into conformations was achieved by the homeomorphic transformation. It used the topological constraint to transform a twist deformation into bending one, which enabled reconfiguration of a simple two-dimensional structure to the three-dimensional supercoiled DNA origami structures. In both methods, local flexibility adjusted by gaps was engineered to relax mechanical stress for a wider shape controllability and control on a critical concentration for buckling transition between a circle and supercoils, respectively. We investigated the design parameters and the available structural shapes in both design methods by a comprehensive set of experiments.

In case of static structures, conformational changes due to the mechanical stress were predicted by a computational shape prediction platform based on FEA. It accelerated the design and validation process providing insight to structural design. Even, it can be extended to development of an automatic design algorithm that can provide sequences for construction of the target 3D curves, which would be our future work. Since our methods are scalable and easily addressable, a number of promising applications are expected when the fine twist control or the continuous

shape transformation could enhance the performance of functional DNA origami structures. Examples can include a biosensor with high sensitivity, a plasmonic device with engineered properties, a smart drug carrier for therapeutics, and dynamic substrate for reorganization of functional materials.

Appendix

A1. Calculation of twist angles of 6HB structures

To compare twist angles of different 6HB structures, first, we defined cell arrays separated by neighboring crossover planes existing at every 7-BP-long distance in the honeycomb lattice (Fig. A1-1). For each cell array, six vertices are obtained by averaging center coordinates of BPs in each helix. They are used to define a representative plane of each cell, which has the smallest sum of distances between each vertex and the plane. For each cell array, then, a triad of unit vectors ($\vec{t}_{i,j}$ | i = 1,2,3, where j represents an index of array cells) can be defined by an auxiliary vector ($\vec{t}_{0,j}$) that connects vertices of helix 1 and 4 and a normal vector of the plane ($\vec{t}_{n,j}$) using following relations

$$\vec{t}_{3,j} = \vec{t}_{n,j} \tag{1}$$

$$\vec{t}_{2,j} = \vec{t}_{3,j} \times \vec{t}_{0,j} \tag{2}$$

$$\vec{t}_{1,j} = \vec{t}_{2,j} \times \vec{t}_{3,j} \tag{3}$$

A rotation matrix (R) between neighboring cell arrays can be calculated using a following relation

$$\left[\vec{t}_{1,j+1} \quad \vec{t}_{2,j+1} \quad \vec{t}_{3,j+1}\right] = R^{j}\left[\vec{t}_{1,j} \quad \vec{t}_{2,j} \quad \vec{t}_{3,j}\right] \tag{4}$$

Then, a quaternion ($\vec{q}$) corresponding to R can be obtained as

$$\vec{q} = [q_r \quad q_1 \quad q_2 \quad q_3] \qquad (5)$$

where $q_r = \frac{1}{2}\sqrt{1 + R^j_{11} + R^j_{22} + R^j_{33}}$, $q_1 = \frac{1}{4q_r}\sqrt{R^j_{32} - R^j_{23}}$, $q_2 = \frac{1}{4q_r}\sqrt{R^j_{13} - R^j_{31}}$ and $q_1 = \frac{1}{4q_r}\sqrt{R^j_{21} - R^j_{12}}$ and R^j_{kl} is a component of R^j. Finally, The local twist angle between neighboring cell arrays (θ) can be finally calculated as following

$$\theta = 2\cos^{-1}(q_r) \qquad . \qquad (6)$$

Similarly, we measured a twist rate of a unit block by it by calculating twist angle between sequential, three cell arrays. And the total twist angle of a structure was calculated by summing twist rates of all unit blocks comprising the structure. The proposed method can be easily extended to other twisted DNA structures with the different number of helices or the different lattice.

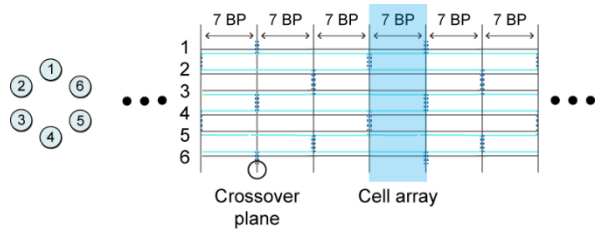

Figure A1-1. Scheme for cell array definition. At every 7-BP-long distance, cell arrays, separated by neighboring crossover planes, are assumed. A representative plane of each cell was defined by averaging center coordinates of BPs in each helix.

A2. Relation between twist angle and trans-ratio (TR)

We calculated the twist angles of folded structures using CanDo and converted them into TR values using a simple geometrical model[53]. To this end, we used the equation derived in the previous study by Lee. et al. (Fig. 2-14).[31] In fact, it referred to an equation derived by Chen. et al.[53] and slightly modified the equation to consider broader twist angles since the original equation only can be applied in the range of [-π, π]. Lee. et al.[31] provides the equation that relates a twist angle (θ_0) of 6hb and TR as a following equation,

$$TR(\theta_0) = \sum_k \left\{ \begin{array}{l} -\frac{\sigma}{\pi\sqrt{2\pi}}\left[\exp\left(-\frac{(2k\pi+\pi-\theta_0)^2}{2\sigma^2}\right) - 2\exp\left(-\frac{(2k\pi-\theta_0)^2}{2\sigma^2}\right) + \exp\left(-\frac{(2k\pi-\pi-\theta_0)^2}{2\sigma^2}\right)\right] \\ +\left(\frac{\sigma_0}{2\pi} - k\right)\left[\mathrm{erf}\left(\frac{2k\pi+\pi-\theta_0}{\sigma\sqrt{2}}\right) - 2\mathrm{erf}\left(\frac{2k\pi-\theta_0}{\sigma\sqrt{2}}\right) + \mathrm{erf}\left(\frac{2k\pi-\pi-\theta_0}{\sigma\sqrt{2}}\right)\right] \end{array} \right\} \quad (7)$$

$$\sigma = \sqrt{\frac{k_B T}{k_t}} = \sqrt{\frac{k_B T}{\frac{L_P k_B T}{L_C}}} = \sqrt{\frac{L_C}{L_P}} = 0.7423 \ \text{rad} \quad (8)$$

where k_B is the Boltzmann constant, T is the absolute temperature, k_t is the torsiona l stiffness of 6HB, L_C is the length of 6HB (= 293 nm) and L_P is the torsional pers istence length (= 530 nm), which was provided in the previous single molecule exp eriment.[28]

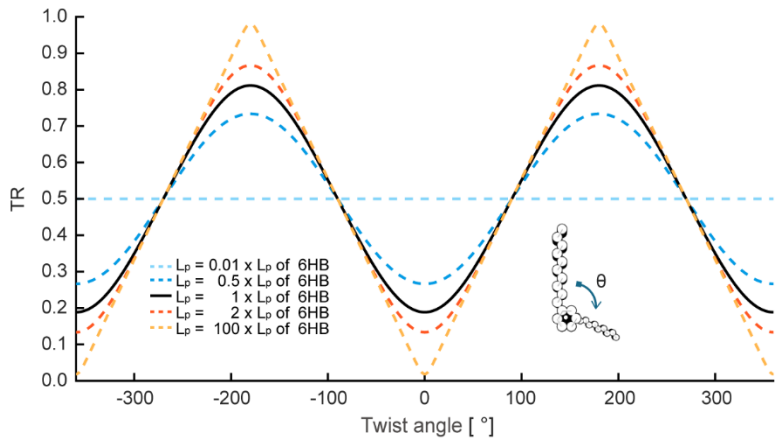

Figure A2-1. Relation between twist angle and trans-ratio (TR). The graph, obtained from Equation 7, showed TR values for various torsional flexibilities and twist angles. When the bundle is assumed to be perfectly rigid, TR is determined purely by the twist angle and ranging from 0 to 1 linearly. When the bundle is extremely flexible, on the opposite limit, TR value becomes always 0.5 regardless of the twist angle. Therefore, this experimental method would be better suited for stiffer structures than softer ones.

A3. FE simulation of a coiling of a dsDNA ring

Due to large displacement and buckling instability, FE simulation for a transition from a circle to coils poses high nonlinearity making it difficult to solve it successfully. To guaranee convergence of the nonlinear analysis, thus, we simplied the 6HB ring into a dsDNA ring consisting of 336 BPs.

Each BP was abstracted into a node and two consecutive BPs were connected by a beam element. The dsDNA was assumed to be intrisically straight and have the regular B-DNA geometry (axial rise of 0.34 nm and helicity of 10.5 BP/turn) with stretch modulus (S) of 1100 pN, bending rigidity (B) of 230 pN nm^2, and torsional rigidity (C) of 460 pN nm^2.

The dsDNA ring was constructed by joining both ends of a straight line representing 336-BP-long dsDNAs. Unwinding of dsDNA due to EtBr binding was considered by making beam elements stress-free when slightly left-handed twisted while a straight beam with no intrinsic twist represents the regular B-DNA twist angle.

To consider conformational changes of a dsDNA due to EtBr binding, a twist angle (θ) was decreased after forming a dsDNA ring with the regular B-DNA geometry. Since both ends are constrained, geometrical perturbations due to change in twist angle cause internal mechanical stress in the ring, which is a driving force for conformational changes. Decreasing a twist angle (θ) between neighboring BPs from 34.29º/BP to 33.32º/BP, about 3%, we calculated the equilibrium conformations and their strain energy (Fig. 3-10A) through nonlinear static FE analysis with only geometrical nonlinearity. FE analysis was performed using the in-

house three dimensional co-rotational beam element[71] codes. Since contact between beam elements was not taken into consideration, our analysis was performed only until contact occurred.

For each step, we calculated a total twist of the dsDNA ring by summing a twist angle along its axial axis. Considering the invariant property of linking number in a closed ring, writhe can be computed as a negative values of twist.

Bibliography

(1) Watson, J. D.; Crick, F., A Structure for Deoxyribose Nucleic Acid. **1953**.

(2) Seeman, N. C., Nucleic Acid Junctions and Lattices. **1982,** *99*, 237-247.

(3) Rothemund, P. W. K., Folding DNA to Create Nanoscale Shapes and Patterns. *Nature* **2006,** *440*, 297-302.

(4) Shih, W. M.; Quispe, J. D.; Joyce, G. F. J. N., A 1.7-Kilobase Single-Stranded DNA That Folds into a Nanoscale Octahedron. **2004,** *427*, 618.

(5) Douglas, S. M.; Dietz, H.; Liedl, T.; Högberg, B.; Graf, F.; Shih, W. M., Self-Assembly of DNA into Nanoscale Three-Dimensional Shapes. *Nature* **2009,** *459*, 414-418.

(6) Ke, Y.; Douglas, S. M.; Liu, M.; Sharma, J.; Cheng, A.; Leung, A.; Liu, Y.; Shih, W. M.; Yan, H., Multilayer DNA Origami Packed on a Square Lattice. *J. Am. Chem. Soc.* **2009,** *131*, 15903-15908.

(7) Rinker, S.; Ke, Y.; Liu, Y.; Chhabra, R.; Yan, H., Self-Assembled DNA Nanostructures for Distance-Dependent Multivalent Ligand–Protein Binding. *Nat. Nanotechnol.* **2008,** *3*, 418.

(8) Nickels, P. C.; Wünsch, B.; Holzmeister, P.; Bae, W.; Kneer, L. M.; Grohmann, D.; Tinnefeld, P.; Liedl, T. J. S., Molecular Force Spectroscopy with a DNA Origami–Based Nanoscopic Force Clamp. **2016,** *354*, 305-307.

(9) Maune, H. T.; Han, S.-p.; Barish, R. D.; Bockrath, M.; Goddard III, W. A.;

Rothemund, P. W.; Winfree, E. J. N. n., Self-Assembly of Carbon Nanotubes into Two-Dimensional Geometries Using DNA Origami Templates. **2010,** *5*, 61.

(10) Liu, J.; Geng, Y.; Pound, E.; Gyawali, S.; Ashton, J. R.; Hickey, J.; Woolley, A. T.; Harb, J. N. J. A. N., Metallization of Branched DNA Origami for Nanoelectronic Circuit Fabrication. **2011,** *5*, 2240-2247.

(11) Kuzyk, A.; Schreiber, R.; Fan, Z.; Pardatscher, G.; Roller, E.-M.; Högele, A.; Simmel, F. C.; Govorov, A. O.; Liedl, T., DNA-Based Self-Assembly of Chiral Plasmonic Nanostructures with Tailored Optical Response. *Nature* **2012,** *483*, 311-314.

(12) Gopinath, A.; Miyazono, E.; Faraon, A.; Rothemund, P. W. J. N., Engineering and Mapping Nanocavity Emission Via Precision Placement of DNA Origami. **2016,** *535*, 401.

(13) Douglas, S. M.; Bachelet, I.; Church, G. M. J. S., A Logic-Gated Nanorobot for Targeted Transport of Molecular Payloads. **2012,** *335*, 831-834.

(14) Iinuma, R.; Ke, Y.; Jungmann, R.; Schlichthaerle, T.; Woehrstein, J. B.; Yin, P. J. s., Polyhedra Self-Assembled from DNA Tripods and Characterized with 3d DNA-Paint. **2014,** *344*, 65-69.

(15) Woo, S.; Rothemund, P. W. J. N. c., Programmable Molecular Recognition Based on the Geometry of DNA Nanostructures. **2011,** *3*, 620.

(16) Gerling, T.; Wagenbauer, K. F.; Neuner, A. M.; Dietz, H. J. S., Dynamic DNA Devices and Assemblies Formed by Shape-Complementary, Non–Base Pairing 3d Components. **2015,** *347*, 1446-1452.

(17) Wagenbauer, K. F.; Sigl, C.; Dietz, H., Gigadalton-Scale Shape-Programmable DNA Assemblies. *Nature* **2017,** *552*, 78-83.

(18) Sobczak, J.-P. J.; Martin, T. G.; Gerling, T.; Dietz, H. J. S., Rapid Folding of DNA into Nanoscale Shapes at Constant Temperature. **2012,** *338*, 1458-1461.

(19) Wagenbauer, K. F.; Engelhardt, F. A.; Stahl, E.; Hechtl, V. K.; Stömmer, P.; Seebacher, F.; Meregalli, L.; Ketterer, P.; Gerling, T.; Dietz, H. J. C., How We Make DNA Origami. **2017,** *18*, 1873-1885.

(20) Bustamante, C.; Smith, S. B.; Liphardt, J.; Smith, D. J. C. o. i. s. b., Single-Molecule Studies of DNA Mechanics. **2000,** *10*, 279-285.

(21) Gore, J.; Bryant, Z.; Nöllmann, M.; Le, M. U.; Cozzarelli, N. R.; Bustamante, C., DNA Overwinds When Stretched. *Nature* **2006,** *442*, 836-839.

(22) Nomidis, S. K.; Kriegel, F.; Vanderlinden, W.; Lipfert, J.; Carlon, E. J. P. r. l., Twist-Bend Coupling and the Torsional Response of Double-Stranded DNA. **2017,** *118*, 217801.

(23) Mao, C.; Sun, W.; Seeman, N. C., Designed Two-Dimensional DNA Holliday Junction Arrays Visualized by Atomic Force Microscopy. *J. Am. Chem. Soc.* **1999,** *121*, 5437-5443.

(24) Murchie, A. I.; Clegg, R. M.; von Krtzing, E.; Duckett, D. R.; Diekmann, S.; Lilley, D. M., Fluorescence Energy Transfer Shows That the Four-Way DNA Junction Is a Right-Handed Cross of Antiparallel Molecules. *Nature* **1989,** *341*, 763-766.

(25) von Kitzing, E.; Lilley, D. M.; Diekmann, S., The Stereochemistry of a Four-Way DNA Junction: A Theoretical Study. *Nucleic Acids Res.* **1990,** *18*, 2671-2683.

(26) Yoo, J.; Aksimentiev, A., In Situ Structure and Dynamics of DNA Origami Determined through Molecular Dynamics Simulations. *Proc. Natl. Acad. Sci. U.S.A.* **2013,** *110*, 20099-20104.

(27) Kim, Y.-J.; Lee, C.; Lee, J. G.; Kim, D.-N. J. A. n., Configurational Design of Mechanical Perturbation for Fine Control of Twisted DNA Origami Structures. **2019**.

(28) Kauert, D. J.; Kurth, T.; Liedl, T.; Seidel, R., Direct Mechanical Measurements Reveal the Material Properties of Three-Dimensional DNA Origami. *Nano Lett.* **2011,** *11*, 5558-5563.

(29) Chen, H.; Weng, T.-W.; Riccitelli, M. M.; Cui, Y.; Irudayaraj, J.; Choi, J. H. J. J. o. t. A. C. S., Understanding the Mechanical Properties of DNA Origami Tiles and Controlling the Kinetics of Their Folding and Unfolding Reconfiguration. **2014,** *136*, 6995-7005.

(30) Kim, Y.-J.; Kim, D.-N., Sensitivity Analysis for the Mechanical Properties of DNA Bundles. *J. Nanomater.* **2016,** *2016*, 6287937.

(31) Lee, J. Y.; Kim, Y.-J.; Lee, C.; Lee, J. G.; Yagyu, H.; Tabata, O.; Kim, D.-N., Investigating the Sequence-Dependent Mechanical Properties of DNA Nicks for Applications in Twisted DNA Nanostructure Design. *Nucleic Acids Res.* **2018,** *47*, 93-102.

(32) Lee, C.; Kim, K. S.; Kim, Y.-J.; Lee, J. Y.; Kim, D.-N. J. A. n., Tailoring the Mechanical Stiffness of DNA Nanostructures Using Engineered Defects. **2019,** *13*, 8329-8336.

(33) Liedl, T.; Högberg, B.; Tytell, J.; Ingber, D. E.; Shih, W. M. J. N. n., Self-Assembly of Three-Dimensional Prestressed Tensegrity Structures from DNA. **2010,** *5*, 520.

(34) Zhou, L.; Marras, A. E.; Su, H.-J.; Castro, C. E., DNA Origami Compliant Nanostructures with Tunable Mechanical Properties. *ACS Nano* **2013,** *8*, 27-34.

(35) Lee, C.; Lee, J. Y.; Kim, D.-N., Polymorphic Design of DNA Origami Structures through Mechanical Control of Modular Components. *Nat. Commun.* **2017,** *8*, 2067.

(36) Benson, E.; Mohammed, A.; Gardell, J.; Masich, S.; Czeizler, E.; Orponen, P.; Högberg, B. J. N., DNA Rendering of Polyhedral Meshes at the Nanoscale. **2015,** *523*, 441.

(37) Veneziano, R.; Ratanalert, S.; Zhang, K.; Zhang, F.; Yan, H.; Chiu, W.; Bathe, M. J. S., Designer Nanoscale DNA Assemblies Programmed from the Top Down. **2016,** *352*, 1534-1534.

(38) Jun, H.; Shepherd, T. R.; Zhang, K.; Bricker, W. P.; Li, S.; Chiu, W.; Bathe, M. J. A. n., Automated Sequence Design of 3d Polyhedral Wireframe DNA Origami with Honeycomb Edges. **2019,** *13*, 2083-2093.

(39) Jun, H.; Zhang, F.; Shepherd, T.; Ratanalert, S.; Qi, X.; Yan, H.; Bathe, M. J. S. a., Autonomously Designed Free-Form 2d DNA Origami. **2019,** *5*, eaav0655.

(40) Snodin, B. E.; Randisi, F.; Mosayebi, M.; Šulc, P.; Schreck, J. S.; Romano, F.; Ouldridge, T. E.; Tsukanov, R.; Nir, E.; Louis, A. A. J. T. J. o. c. p., Introducing Improved Structural Properties and Salt Dependence into a Coarse-Grained Model of DNA. **2015,** *142*, 06B613_1.

(41) Castro, C. E.; Kilchherr, F.; Kim, D.-N.; Shiao, E. L.; Wauer, T.; Wortmann, P.; Bathe, M.; Dietz, H., A Primer to Scaffolded DNA Origami. *Nat. Methods* **2011,** *8*, 221-229.

(42) Kim, D.-N.; Kilchherr, F.; Dietz, H.; Bathe, M., Quantitative Prediction of 3d Solution Shape and Flexibility of Nucleic Acid Nanostructures. *Nucleic Acids Res.* **2011,** *40*, 2862-2868.

(43) Pan, K.; Kim, D.-N.; Zhang, F.; Adendorff, M. R.; Yan, H.; Bathe, M., Lattice-Free Prediction of Three-Dimensional Structure of Programmed DNA Assemblies. *Nat. Commun.* **2014,** *5*, 5578.

(44) Ke, Y.; Voigt, N. V.; Gothelf, K. V.; Shih, W. M., Multilayer DNA Origami Packed on Hexagonal and Hybrid Lattices. *J. Am. Chem. Soc.* **2012,** *134*, 1770-1774.

(45) Zhang, F.; Jiang, S.; Wu, S.; Li, Y.; Mao, C.; Liu, Y.; Yan, H. J. N. n., Complex Wireframe DNA Origami Nanostructures with Multi-Arm Junction Vertices. **2015,** *10*, 779.

(46) Benson, E.; Mohammed, A.; Bosco, A.; Teixeira, A. I.; Orponen, P.; Högberg, B. J. A. C. I. E., Computer-Aided Production of Scaffolded DNA Nanostructures from Flat Sheet Meshes. **2016,** *55*, 8869-8872.

(47) Marras, A. E.; Zhou, L.; Su, H.-J.; Castro, C. E. J. P. o. t. N. A. o. S., Programmable Motion of DNA Origami Mechanisms. **2015,** *112*, 713-718.

(48) Zhou, L.; Marras, A. E.; Huang, C. M.; Castro, C. E.; Su, H. J. J. S., Paper Origami-Inspired Design and Actuation of DNA Nanomachines with Complex Motions. **2018,** *14*, 1802580.

(49) Dietz, H.; Douglas, S. M.; Shih, W. M., Folding DNA into Twisted and Curved Nanoscale Shapes. *Science* **2009,** *325*, 725-730.

(50) Maier, A. M.; Bae, W.; Schiffels, D.; Emmerig, J. F.; Schiff, M.; Liedl, T., Self-Assembled DNA Tubes Forming Helices of Controlled Diameter and Chirality. *ACS Nano* **2017,** *11*, 1301-1306.

(51) Chen, H.; Li, R.; Li, S.; Andréasson, J.; Choi, J. H., Conformational Effects of Uv Light on DNA Origami. *J. Am. Chem. Soc.* **2017,** *139*, 1380-1383.

(52) Wang, J. J. J. o. m. b., The Degree of Unwinding of the DNA Helix by Ethidium: I. Titration of Twisted Pm2 DNA Molecules in Alkaline

Cesium Chloride Density Gradients. **1974,** *89*, 783-801.

(53) Chen, H.; Zhang, H.; Pan, J.; Cha, T.-G.; Li, S.; Andréasson, J.; Choi, J. H., Dynamic and Progressive Control of DNA Origami Conformation by Modulating DNA Helicity with Chemical Adducts. *ACS Nano* **2016,** *10*, 4989-4996.

(54) Zadegan, R. M.; Lindau, E. G.; Klein, W. P.; Green, C.; Graugnard, E.; Yurke, B.; Kuang, W.; Hughes, W. L., Twisting of Dna Origami from Intercalators. *Sci. Rep.* **2017,** *7*, 7382.

(55) Zhao, Y.-X.; Shaw, A.; Zeng, X.; Benson, E.; Nyström, A. M.; Högberg, B. r., DNA Origami Delivery System for Cancer Therapy with Tunable Release Properties. *ACS Nano* **2012,** *6*, 8684-8691.

(56) Siavashpouri, M.; Wachauf, C. H.; Zakhary, M. J.; Praetorius, F.; Dietz, H.; Dogic, Z., Molecular Engineering of Chiral Colloidal Liquid Crystals Using DNA Origami. *Nat. Mater.* **2017,** *16*, 849-856.

(57) Wang, P.; Gaitanaros, S.; Lee, S.; Bathe, M.; Shih, W. M.; Ke, Y., Programming Self-Assembly of DNA Origami Honeycomb Two-Dimensional Lattices and Plasmonic Metamaterials. *J. Am. Chem. Soc.* **2016,** *138*, 7733-7740.

(58) Zimmermann, E. A.; Gludovatz, B.; Schaible, E.; Dave, N. K.; Yang, W.; Meyers, M. A.; Ritchie, R. O., Mechanical Adaptability of the Bouligand-Type Structure in Natural Dermal Armour. *Nat. Commun.* **2013,** *4*, 2634.

(59) Zhang, M.; Atkinson, K. R.; Baughman, R. H., Multifunctional Carbon

Nanotube Yarns by Downsizing an Ancient Technology. *Science* **2004,** *306*, 1358-1361.

(60) Pan, N.; Brookstein, D., Physical Properties of Twisted Structures. Ii. Industrial Yarns, Cords, and Ropes. *J. Appl. Polym. Sci.* **2002,** *83*, 610-630.

(61) Frenzel, T.; Kadic, M.; Wegener, M., Three-Dimensional Mechanical Metamaterials with a Twist. *Science* **2017,** *358*, 1072-1074.

(62) Foroughi, J.; Spinks, G. M.; Wallace, G. G.; Oh, J.; Kozlov, M. E.; Fang, S.; Mirfakhrai, T.; Madden, J. D.; Shin, M. K.; Kim, S. J., Torsional Carbon Nanotube Artificial Muscles. *Science* **2011,** *334*, 494-497.

(63) Bai, X.-c.; Martin, T. G.; Scheres, S. H.; Dietz, H., Cryo-Em Structure of a 3d DNA-Origami Object. *Proc. Natl. Acad. Sci. U.S.A.* **2012,** *109*, 20012-20017.

(64) Lu, X. J.; Olson, W. K., 3dna: A Software Package for the Analysis, Rebuilding and Visualization of Three-Dimensional Nucleic Acid Structures. *Nucleic Acids Res.* **2003,** *31*, 5108-5121.

(65) Funke, J. J.; Dietz, H., Placing Molecules with Bohr Radius Resolution Using DNA Origami. *Nat. Nanotechnol.* **2016,** *11*, 47-52.

(66) Douglas, S. M.; Marblestone, A. H.; Teerapittayanon, S.; Vazquez, A.; Church, G. M.; Shih, W. M., Rapid Prototyping of 3d DNA-Origami Shapes with Cadnano. *Nucleic Acids Res.* **2009,** *37*, 5001-5006.

(67) Biebricher, A. S.; Heller, I.; Roijmans, R. F.; Hoekstra, T. P.; Peterman,

E. J.; Wuite, G. J. J. N. c., The Impact of DNA Intercalators on DNA and DNA-Processing Enzymes Elucidated through Force-Dependent Binding Kinetics. **2015,** *6*, 7304.

(68) Goriely, A. J. J. o. E., Twisted Elastic Rings and the Rediscoveries of Michell's Instability. **2006,** *84*, 281-299.

(69) Lipfert, J.; Klijnhout, S.; Dekker, N. H. J. N. a. r., Torsional Sensing of Small-Molecule Binding Using Magnetic Tweezers. **2010,** *38*, 7122-7132.

(70) Yang, Y.; Endo, M.; Hidaka, K.; Sugiyama, H. J. J. o. t. A. C. S., Photo-Controllable DNA Origami Nanostructures Assembling into Predesigned Multiorientational Patterns. **2012,** *134*, 20645-20653.

(71) Battini, J.-M.; Pacoste, C. J. C. M. i. A. M.; Engineering, Co-Rotational Beam Elements with Warping Effects in Instability Problems. **2002,** *191*, 1755-1789.

국 문 초 록

본 학위논문은 목표하는 정적 및 동적 형상을 지닌 DNA 오리가미 구조 제작을 위한 기계적 응력 조절 기술에 기반한 설계방법을 제시한다. DNA 오리가미 나노기술은 DNA 가닥들의 자가조립 과정을 통해 기존에 제작이 어려웠던 다양한 형상의 나노구조물을 손쉽게 만들 수 만들 수 있다. 이를 활용해 목표 형상의 나노구조물을 만들기 위해 다양한 설계 방법들이 제시되어 왔다. 이중 역학적 원리에 기반한 설계 방법은 구조 내부에 의도적으로 기계적 스트레스를 발생시켜 구조의 비틀림, 굽힘 등을 정량적으로 조절할 수 있게 만들어, 제작 가능한 형상의 범주를 넓히는데 크게 기여하였다. 하지만 기존 방법들은 세밀한 비틀림 형상 제어가 어렵다는 점 그리고 제한된 종류의 형상변화만이 가능하다는 문제점으로 인해 목표 형상을 지닌 정적 혹은 동적 구조의 제작 및 이러한 구조들의 활용에 어려움이 존재한다. 이에 해결책으로써 본 연구는 다음과 같은 기계적 응력 조절 기술들을 제시한다. 첫째, 구조 내 기하학적 섭동의 분포 설계 통해 DNA 오리가미 구조물의 세밀한 비틀림 형상 조절을 위한 설계 방법을 제시한다. 이를 이용한 구조 내 변형 에너지의 조절을 통해, 미세한 비틀림 형상 조절이 가능해진다. 둘째, 단순한 2차원 구조물을 복잡한 3차원 형상의 구조물로 변환시키는 형상 변환 메커니즘을 제안한다. 양끝이 이어진 닫힌 구조가 지닌 위상학적 불변성을 이용해, 국부적 비틀림을 전역적 굽힘 변형으로 변환시킴으로써, DNA 오리가미 구조의 슈퍼코일링 현상을 제시한다. 이러한 기계적 응력 조절 기술들은 원하는 형상 및 변화 움직임을 지닌 DNA 나노구조물의 설계에 활용되어 기능성 나노구조물들의 성능을 향상시키는데 기여할 것이라고 기대된다.

주요어 : DNA 오리가미, DNA 나노구조체, 기계적 응력 조절 기술, 비틀림 형상 제어, 나노구조체의 형상 변화, 기계적 불안정성

학　　번 : 2013-20654

Acknowledgments

I would first like to express my deep gratitude to my advisor, Prof. Do-Nyun Kim, for supporting me during the doctoral course, and giving me the freedom to pursue my own ideas. I really enjoyed the discussion with him due to his invaluable guidance and encouragements for researches. I look forward to continued collaboration in the future. I am also grateful to my committee members, Prof. Yoon Young Kim, Prof. Maenghyo Cho, Prof. Yongdae Shin, and Prof. Jin-Gyun Kim for their excellent suggestions and comments on my research during PhD.

My colleagues in the Simulation-driven Structure Design Laboratory have played a key role during my graduate studies. Both weekly team meetings and lab seminars were invaluable. Especially, Chanseok Lee, Jae Young Lee, Jae Gyung Lee, Kyung Soo Kim, Tae Hwi Kim, and Joonho Park, all of whom I gratefully acknowledge here with my sincere thanks for fruitful discussions.

Also, I would like to express my deepest gratitude to my family and friends who supported me throughout my PhD. They have been a constant source of love and strength over the years, I look forward to quality time with all of them. This dissertation would without a doubt not have been possible without my wife, Yeseul. Your love, trust and encouragement kept me going. With your support everything is within reach. You and our son, Joonseo, enrich my life, every day.

Finally, thank God for giving me the pleasure of research. I pray that you will continue to lead my life, forever.